

# X-ray Absorption Linear Dichroism at the Ti K-edge of TiO<sub>2</sub> anatase single crystal

T. C. Rossi<sup>1</sup>, D. Grolimund<sup>2</sup>, M. Nachtegaal<sup>3</sup>, O. Cannelli<sup>1,4</sup>,  
G. F. Mancini<sup>1,4</sup>, C. Bacellar<sup>1,4</sup>, D. Kinschel<sup>1,4</sup>, J. Rouxel<sup>1,4</sup>,  
N. Ohannessian<sup>6</sup>, D. Pergolesi<sup>5,6</sup>, T. Lippert<sup>6,7</sup>, M. Chergui<sup>1</sup>

<sup>1</sup>*Laboratory of Ultrafast Spectroscopy,  
Ecole Polytechnique Fédérale de Lausanne SB-ISIC,  
and Lausanne Centre for Ultrafast Science (LACUS),  
Station 6, Lausanne, CH-1015, Switzerland*

<sup>2</sup>*Laboratory for Femtochemistry - MicroXAS beamline project,  
Paul Scherrer Institute, Villigen, CH-5232, Switzerland*

<sup>3</sup>*Bioenergy and Catalysis Laboratory,  
Paul Scherrer Institute, Villigen, CH-5232, Switzerland*

<sup>4</sup>*Paul Scherrer Institute, 5232 PSI Villigen, Switzerland*

<sup>5</sup>*Electrochemistry Laboratory, Paul Scherrer Institute, Villigen, CH-5232, Switzerland*

<sup>6</sup>*Laboratory for Multiscale Materials Experiments,  
Paul Scherrer Institute, Villigen, CH-5232, Switzerland*

<sup>7</sup>*Department of Chemistry and Applied Biosciences,  
Laboratory of Inorganic Chemistry, ETH Zürich,  
Vladimir-Prelog-Weg 1-5/10, 8093 Zürich, Switzerland*

(Dated: April 24, 2019)

## Abstract

Anatase  $\text{TiO}_2$  (a- $\text{TiO}_2$ ) exhibits a strong X-ray absorption linear dichroism with the X-ray incidence angle in the pre-edge, the XANES and the EXAFS at the titanium K-edge. In the pre-edge region the behaviour of the A1-A3 and B peaks, originating from the 1s-3d transitions, is due to the strong  $p$ -orbital polarization and strong  $p-d$  orbital mixing. An unambiguous assignment of the pre-edge peak transitions is made in the mono-electronic approximation with the support of *ab initio* finite difference method calculations and spherical tensor analysis in quantitative agreement with the experiment. It is found that A1 is mostly an on-site 3d-4p hybridized transition, while peaks A3 and B are non-local transitions, with A3 being mostly dipolar and influenced by the 3d-4p intersite hybridization, while B is due to interactions at longer range. Finally, peak A2 which was previously assigned to a transition involving pentacoordinated titanium atoms exhibits a quadrupolar angular evolution with incidence angle. These results pave the way to the use of the pre-edge peaks at the K-edge of a- $\text{TiO}_2$  to characterize the electronic structure of related materials and in the field of ultrafast X-ray absorption spectroscopy (XAS) where the linear dichroism can be used to compare the photophysics along different axes.

## INTRODUCTION

Titanium dioxide ( $\text{TiO}_2$ ) is one of the most studied large-gap semiconductor due to its present and potential applications in photovoltaics [1] and photocatalysis [2]. The increasingly strict requirements of modern devices call for sensitive material characterization techniques which can provide local insights at the atomic level [3, 4]. K-edge X-ray absorption spectroscopy (XAS) is an element specific technique, that is used to extract the local geometry around an atom absorbing the X-radiation, as well as about its electronic structure [5]. A typical absorption K-edge is usually composed of three parts: (i) in the high energy region above the absorption edge (typically  $> 50$  eV), the extended X-ray absorption fine structure (EXAFS), contains information about bond distances. Modelling of the EXAFS is rather straightforward, as the theory is well established [5]; (ii) The edge region and slightly above it ( $< 50$  eV) represents the X-ray absorption near edge structure (XANES), which contains information about bond distances and bond angles around the absorbing atom, as well as about its oxidation state. In contrast to EXAFS, XANES features require more complex theoretical developments due to the multiple scattering events and their interplay with bound-bound atomic transitions; (iii) The pre-edge region consists of bound-bound transitions of the absorbing atom. In the case of transition metals, the final states are partially made of  $d$ -orbitals. Pre-edge transitions thus deliver information about orbital occupancies and about the local geometry because the dipole-forbidden  $s$ - $d$  transitions are relaxed by lowering of the local symmetry. The Ti K-edge absorption spectrum of anatase  $\text{TiO}_2$  (a- $\text{TiO}_2$ ) exhibits four pre-edge features labelled A1, A2, A3 and B (see Figure 2a), while rutile  $\text{TiO}_2$  only shows three [6, 7]. Their assignment has been at the centre of a long debate, which is still going on, especially in the case of the a- $\text{TiO}_2$  polymorph [8–10]. A summary of the assignment of pre-edge transitions from previous works is given in Table I, which we now comment.

Early theoretical developments to explain the origin of pre-edge features in a- $\text{TiO}_2$  were based on molecular orbital (MO) theory [11–13] which showed that the first two empty states in a- $\text{TiO}_2$  are made of antibonding  $t_{2g}$  and  $e_g$  orbitals derived from the  $3d$  atomic orbitals of Ti. Transitions to these levels have, respectively, been assigned to the A3 and B peaks while the absorption edge is made of Ti  $t_{1u}$  antibonding orbitals derived from Ti  $4p$  atomic orbitals. Although MO theory can predict the energy position of the transitions accurately,

it cannot compute the corresponding cross-sections and does not account for the core-hole to which quadrupolar transitions to  $d$ -orbitals at the K-edge are extremely sensitive [9]. The corresponding transitions are usually red shifted by the core-hole and appear as weak peaks on the low energy side of the pre-edge. In a-TiO<sub>2</sub>, peak A1 contains a significant quadrupolar component [9], sensitive to the core hole, which explains the inaccuracy of MO theory to predict this transition. Full multiple scattering (FMS) is a suitable technique to treat large ensemble of atoms and obtain accurate cross-sections [8, 10, 12, 14]. From FMS calculations, a consensus has emerged assigning A1 to be of partial quadrupolar character, A3 a mixture of dipolar and quadrupolar character with  $t_{2g}$  orbitals and B, a purely dipolar transition involving  $e_g$  orbitals [12, 15]. However, as correctly pointed out by Ruiz-Lopez [12], this simple picture of octahedral symmetry energy split  $t_{2g}$  and  $e_g$  levels becomes more complicated in a-TiO<sub>2</sub> because of the local distorted octahedral environment ( $D_{2d}$  symmetry) which allows local  $p - d$  orbital hybridization [16]. In that case, the dipolar contribution to the total cross-section becomes dominant for every transition in the pre-edge region [17]. In addition, the cluster size used for the FMS calculations has a large influence on the A3 and B peak intensities showing that delocalized final states (off-site transitions) play a key role in the pre-edge absorption region [12]. Finally, the local environment around Ti atoms in a-TiO<sub>2</sub> is strongly anisotropic and Ti-O bond distances separate in two groups of apical and equatorial oxygens which cannot be correctly described with spherical muffin-tin potentials as implemented in FMS.

Empirical approaches have been used by Chen and co-workers [18] and Luca and co-workers [7, 19, 20] to establish correlations between the Ti K pre-edge transitions in a-TiO<sub>2</sub> and sample morphologies, showing that bond length and static disorder contribute to the change in the pre-edge peak amplitudes [18] and that the A2 peak is due to pentacoordinated Ti atoms [7, 19, 20]. Farges and co-workers confirmed this assignment with the support of multiple scattering (MS) calculations [14]. The recent works by Zhang et al. [21] and Triana et al. [15] have shown the strong interplay between the intensity of pre-edge features and the coordination number and static disorder, in particular in the case of the A2 peak.

The clear assignment of the pre-edge features of a-TiO<sub>2</sub> is important in view of recent steady-state and ultrafast XAS [22–24] and optical experiments [25]. In the picosecond XAS experiments on photoexcited a-TiO<sub>2</sub> nanoparticles above the band gap, a strong enhancement of the A2 peak was observed, along with a red shift of the edge [22]. This was

interpreted as trapping of the electrons transferred to the conduction band at undercoordinated Ti defect centres that are abundant in the shell region of the nanoparticles, turning them from an oxidation of +4 to +3 [22]. The trapping time was determined by femtosecond XAS to be  $< 200$  fs, i.e. the electron is trapped immediately at or near the unit cell where it was created [23, 24]. Further to this, the trapping sites were identified as being due to oxygen vacancies ( $O_{\text{vac}}$ ) in the first shell of the reduced Ti atom. These  $O_{\text{vac}}$ 's are linked to two Ti atoms in the equatorial plane and one Ti atom in the apical position which induces two different responses at the Ti K-edge when a charge gets trapped at an  $O_{\text{vac}}$  [23, 26]. However, these hypotheses await for confirmation based on further experimental and theoretical studies, which for the steady-state case, we present in this article. In particular, the study of the structural rearrangements of photoexcited single crystals is planned in which the first transition at the optical gap has been identified as a 2-dimensional (2D) exciton in the 3D lattice of the material [25]. The robustness of this transition with respect to defects hinted to possible applications in relation to energy and/or charge transport. The time-resolved XAS study of single crystals with a controllable amount of  $O_{\text{vac}}$ 's would be important to clarify these issues.

Recently, there have been two main developments in the computation of XANES spectra. The first is based on band structure calculations (LDA, LDA+U,...), which compute potentials self-consistently before the calculation of the XAS absorption cross-section with a core-hole in the final state [17, 27]. This approach provides excellent accuracy but is limited to the few tens of eV above the absorption edge due to the computational cost of increasing the basis set to include the EXAFS. The second one, the finite difference method for near-edge structure (FDMNES) implemented by Joly [28, 29], overcomes the limitations of the muffin-tin approximation in order to get accurate descriptions of the pre-edge transitions especially for anisotropic materials. The recent theoretical work by Cabaret and coworkers combining GGA-PBE self-consistent calculations with FDMNES [17] concluded that in a-TiO<sub>2</sub>, peak A1 is due to a mixture of quadrupolar ( $t_{2g}$ ) and dipolar transitions ( $p - t_{2g}$ ), A3 to on-site dipolar ( $p - e_g$ ), off-site dipolar ( $p - t_{2g}$ ) and quadrupolar ( $e_g$ ) transitions, while B is due to an off-site dipolar transition ( $p_z - e_g$ ). However, experimental support to the pre-edge assignments is still lacking, and is provided in this work using linear dichroism (LD) XAS at the Ti K-edge of a-TiO<sub>2</sub> with the theoretical support of *ab-initio* full potential FDMNES calculations and spherical harmonics analysis of the XAS cross-section. We show

that A1 is mainly due to dipolar transitions to on-site hybridized  $4p_{x,y} - 3d_{xz}, 3d_{yz}$  final states which gives a strong dipolar LD to the transition with a weak quadrupolar component from  $(3d_{xz}, 3d_{yz}, 3d_{x^2-y^2})$  states. The A3 peak is due to a mixture of dipolar transitions to hybridized  $4p_{x,y,z} - (3d_{xy}, 3d_{z^2})$  final states as a result of strong hybridization with the  $3d$  orbitals of the nearest Ti neighbour with a small quadrupolar component. The B peak is purely dipolar ( $4p$  orbitals in the final state) and is an off-site transition (the electron final state is essentially away from the absorbing atom). Finally, we experimentally observe a quadrupolar evolution of the A2 peak amplitude, in qualitative agreement with the finite difference method (FDM) calculations. We argue that the amplitude of this transition may strongly depend on atomic vacancies which allow orbital mixing via lowered symmetries and may also come from the peak A1 undergoing a blue spectral shift, due to the oxygen vacancy, moving it to the region of peak A2. This explains the relatively intense A2 peak in amorphous  $\text{TiO}_2$  [21] or upon electron trapping at defects after photoexcitation of anatase or rutile  $\text{TiO}_2$  [22, 23, 26].

## EXPERIMENTAL SETUP

### Linear dichroism

The LD measurements are performed at the SuperXAS and microXAS beamlines of the SLS in Villigen, Switzerland using a double Si(311) crystal monochromator to optimize the energy resolution. Energy calibration is performed from the first derivative of the XAS spectrum of a thin Ti foil. We used a moderately focused rectangular-shaped X-ray beam of  $20 \times 200 \mu\text{m}^2$  in horizontal and vertical dimension, respectively. The XAS spectrum is obtained in total fluorescence yield with a Ketek Axas detector system with Vitus H30 SFF and ultra-low capacitance Cube-Asic preamplifier (Ketek GmbH).

The sample consists of a (001)-oriented crystalline a- $\text{TiO}_2$  thin film of 30 nm thickness. Sample growth and characterization procedures are reported in the Supplementary Information (SI) §. Figure 1 shows a schematics of the sample motion required for the experiment. The sample was placed in the center of rotation of a system of stages which allow for both sample in-plane rotation ( $\phi$ ) and orthogonal out-of plane rotation ( $\theta$ ). By convention, a set of Euler angles  $(\theta, \phi, \psi)$  orients the electric field  $\hat{\epsilon}$  and wavevector  $\hat{k}$  with respect to the

sample.  $\theta$  measures the angle between  $\hat{\epsilon}$  and the  $[001]$  crystal direction ( $\hat{z}$  axis of the sample frame) orthogonal to the surface.  $\phi$  measures the angle between  $\hat{\epsilon}$  and the sample rotation axis  $\hat{x}$ . In principle, a third angle  $\psi$  is necessary to fix the position of the wavevector in the orthogonal plane to the electric field but here  $\psi = 0^\circ$ . The  $\theta$  angles reported in the experimental datasets are with a maximum systematic offset of  $\pm 0.2^\circ$  which comes from the precision setting up the  $\theta = 0^\circ$  reference from the sample half-clipping of the X-ray beam at grazing incidence. The precision of the rotation stage of  $\pm 0.01^\circ$  is negligible with respect to this angular offset.

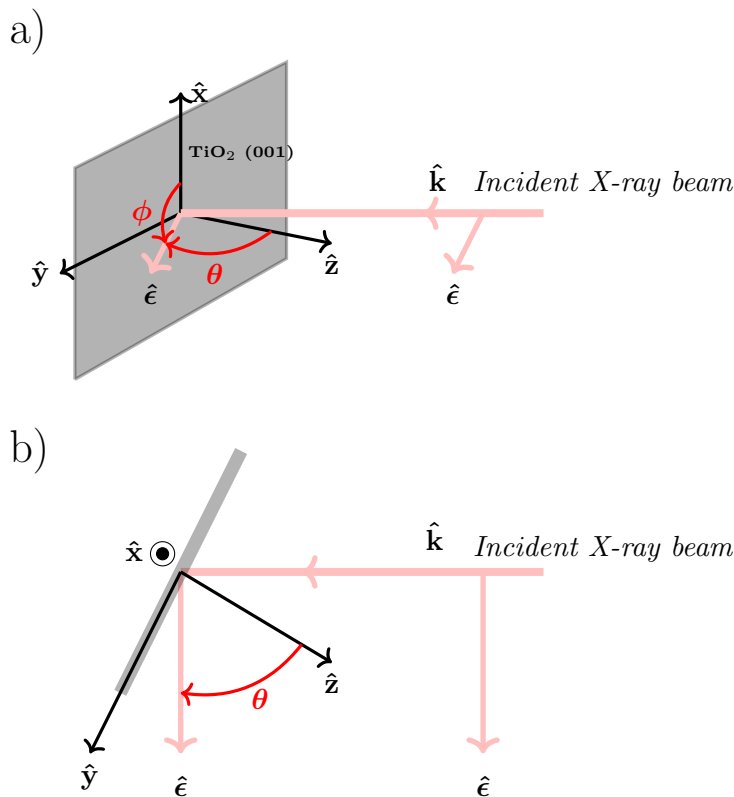


FIG. 1. Linear dichroism experiment with (a) side view and (b) top view. The sample surface is in grey while the incident X-ray beam is in pink. A set of Euler angles  $(\theta, \phi, \psi)$  is used to orient the electric field  $\hat{\epsilon}$  and wavevector  $\hat{k}$  of the incident X-ray beam with respect to the sample.

LD is usually studied with the sample rotated in the plane orthogonal to the incident X-ray beam ( $\phi$ -rotation) [30]. In this work, the novelty comes from the sample rotation around  $\hat{x}$  ( $\theta$ -rotation) which provides the largest changes in the XAS. This rotation induces a change of X-ray footprint onto the sample surface. We clearly show that it does not

introduce spectral distortions because the effective penetration depth of the X-rays through the material (between 2 and 15  $\mu\text{m}$  across the absorption edge of a-TiO<sub>2</sub> for the largest footprint at  $\theta = 1^\circ$  used here [31]) is kept constant as the sample is much thinner than the attenuation length at the Ti K-edge. Instead, the total amount of material probed by the X-rays changes due to the larger X-ray footprint when  $\theta$  increases and a renormalization over the detected number of X-ray fluorescence photons is required. This is done with the support of the FDMNES calculations since a few energy points have  $\theta$ -independent cross-sections as previously reported on other systems [32–38] (*vide infra*)[39]. With this renormalization procedure performed at a single energy point (4988.5 eV), we could obtain a set of experimental points with  $\theta$ -independent cross-sections at the energies predicted by the theory confirming the reliability of the method. Hence, crystalline thin films with suitable thicknesses with respect to the X-ray penetration depth offer more possibilities to study LD effects than single crystals and prevent the usual self-absorption distortion of bulk materials when using total fluorescence yield detection [40].

TABLE I. Previous assignments of the final states involved in the pre-edge transitions of the Ti K-edge spectrum of a-TiO<sub>2</sub>. The orbitals with dominant contribution to the transition are emphasized in bold. *E1* is for dipolar transitions and *E2* for quadrupolar transitions. Off-site transitions are in red, on-site transitions are in black. Irreducible representations corresponding to the final state in the considered point group of a-TiO<sub>2</sub> are in parentheses. The dash "-" symbol refers to orbital hybridization.

reference	A1	A2	A3	B
[10]	<b>3d<sub>x<sup>2</sup>-y<sup>2</sup></sub></b> ( <i>b</i> <sub>1</sub> ), 4 <i>p<sub>x</sub></i> , 4 <i>p<sub>y</sub></i> , 3 <i>d<sub>xz</sub></i> , 3 <i>d<sub>yz</sub></i> ( <i>e</i> )	<b>4p<sub>z</sub></b> , <b>3d<sub>xy</sub></b> ( <i>b</i> <sub>2</sub> ), 4 <i>p<sub>x</sub></i> , 4 <i>p<sub>y</sub></i> , 3 <i>d<sub>xz</sub></i> , 3 <i>d<sub>yz</sub></i> ( <i>e</i> )	<b>4p<sub>z</sub></b> , <b>3d<sub>xy</sub></b> ( <i>b</i> <sub>2</sub> ), 3 <i>d<sub>z<sup>2</sup></sub></i> ( <i>a</i> <sub>1</sub> )	<b>4p</b> , <b>4s</b>
[17]	<i>E1</i> : <b>p</b> ( <b>t<sub>2g</sub></b> ), <i>E2</i> : 3 <i>d</i> ( <i>t<sub>2g</sub></i> )		<i>E1</i> : <b>p</b> ( <b>e<sub>g</sub></b> ), <b>p - 3d</b> ( <b>t<sub>2g</sub></b> ), <i>E2</i> : 3 <i>d</i> ( <i>e<sub>g</sub></i> )	<i>E1</i> : <b>p<sub>z</sub></b> , <b>3d</b> ( <b>e<sub>g</sub></b> )
[15]	<i>E1</i> : <b>4p - 3d</b> ( <b>t<sub>2g</sub></b> ), <i>E2</i> : 3 <i>d</i> ( <i>t<sub>2g</sub></i> )		<i>E1</i> : <b>4p</b> , <b>d<sub>xy</sub></b> , <b>d<sub>xz</sub></b> , <b>d<sub>yz</sub></b> ( <b>t<sub>2g</sub></b> )	<i>E1</i> : <b>4p</b> , <b>d<sub>x<sup>2</sup>-y<sup>2</sup></sub></b> , <b>d<sub>z<sup>2</sup></sub></b> ( <b>e<sub>g</sub></b> )
This work	<i>E1</i> : <b>4p<sub>x,y</sub> - 3d<sub>xz</sub></b> , <b>3d<sub>yz</sub></b> , <i>E2</i> : <i>d<sub>xz</sub></i> , <i>d<sub>yz</sub></i> , <i>d<sub>x<sup>2</sup>-y<sup>2</sup></sub></i>	<i>E2</i> : <b>3d<sub>xy</sub></b> , 3 <i>d<sub>z<sup>2</sup></sub></i>	<i>E1</i> : <b>4p<sub>x</sub></b> , <b>4p<sub>y</sub></b> , <b>4p<sub>z</sub> - 3d<sub>xy</sub></b> , 3 <i>d<sub>z<sup>2</sup></sub></i>	<i>E1</i> : <b>4p<sub>x</sub></b> , <b>4p<sub>y</sub></b> , <b>4p<sub>z</sub></b>

## THEORY

### Finite difference *ab-initio* calculations

The *ab-initio* calculations of the XAS cross-section were performed with the full potential FDM as implemented in the FDMNES package [29, 41]. A cluster of 7.0 Å was used for the

calculation with the fundamental electronic configuration of the oxygen atom and an excited state configuration for the titanium atom (Ti: [Ar]3d<sup>1</sup>4s<sup>2</sup>4p<sup>1</sup>) as performed elsewhere [21]. We checked the convergence of the calculation for increasing cluster sizes and found minor evolution for larger cluster radii than 7.0 Å (123 atoms). The Hedin-Lundqvist exchange-correlation potential is used [42]. A minor adjustment of the screening properties of the 3d levels needs to be used to match the energy position of the pre-edge features with the experiment. We found the best agreement for a screening of 0.85 for the 3d electrons. After the convolution of the spectrum with an arctan function with maximum broadening of 1.5 eV followed by a constant gaussian broadening of 0.095 eV to account for the experimental resolution of the experiment and get the closest agreement with the broadening of the pre-edge peaks.

### Spherical tensor analysis of the dipole and quadrupole cross-sections

Analytical expressions of the dipole and quadrupole XAS cross-sections ( $\sigma^D(\hat{\epsilon})$  and  $\sigma^Q(\hat{\epsilon}, \hat{k})$ , respectively) are obtained from their expansion into spherical harmonic components [30, 43]. The expressions of  $\sigma^D(\hat{\epsilon})$  and  $\sigma^Q(\hat{\epsilon}, \hat{k})$  depend on the crystal point group which is  $D_{4h}$  ( $4/mmm$ ) for a-TiO<sub>2</sub>. The dipole cross-section is given by:

$$\sigma^D(\hat{\epsilon}) = \sigma^D(0, 0) - \frac{1}{\sqrt{2}}(3 \cos^2 \theta - 1)\sigma^D(2, 0) \quad (1)$$

and the quadrupole cross-section by:

$$\begin{aligned} \sigma^Q(\hat{\epsilon}, \hat{k}) = & \sigma^Q(0, 0) + \sqrt{\frac{5}{14}}(3 \sin^2 \theta \sin^2 \psi - 1)\sigma^Q(2, 0) \\ & + \frac{1}{\sqrt{14}}[35 \sin^2 \theta \cos^2 \theta \cos^2 \psi + 5 \sin^2 \theta \sin^2 \psi - 4]\sigma^Q(4, 0) \\ & + \sqrt{5} \sin^2 \theta[(\cos^2 \theta \cos^2 \psi - \sin^2 \psi) \cos 4\phi - 2 \cos \theta \sin \psi \cos \psi \sin 4\phi]\sigma^{Qr}(4, 4) \end{aligned} \quad (2)$$

with  $\theta$ ,  $\phi$  and  $\psi$  as defined in the Ti site point group ( $D_{2d}$ ).  $\sigma^X(l, m)$  with  $X = D, Q$  is the spherical tensor with rank  $l$  and projection  $m$ . The Euler angles  $(\theta, \phi, \psi)$  in the experiment are referenced to the crystal frame which is rotated in the  $(O, \hat{x}, \hat{y})$  plane with respect to the Euler angles in the Ti site frame. Consequently, the angles in equations 1 and 2 differ from the angles defined in Figure 1 by a rotation of  $\phi$ . In the Ti site frame, the  $\hat{x}$  and  $\hat{y}$  axes are bisectors of the Ti–O bonds while the crystal frame is along the bonds. The matrix  $R$  to

go from the site frame to the crystal frame is,

$$R = \begin{pmatrix} \frac{1}{\sqrt{2}} & \frac{1}{\sqrt{2}} & 0 \\ -\frac{1}{\sqrt{2}} & \frac{1}{\sqrt{2}} & 0 \\ 0 & 0 & 1 \end{pmatrix} \quad (3)$$

In the following, the polarizations of  $\hat{\epsilon}$  and  $\hat{k}$  are given in the crystal frame. Consequently, the corresponding polarizations for the site frame are given by  $\hat{\epsilon}_S = R^{-1}(\hat{\epsilon})$  and  $\hat{k}_S = R^{-1}(\hat{k})$ .

Although some terms of  $\sigma^D(\hat{\epsilon})$  and  $\sigma^Q(\hat{\epsilon}, \hat{k})$  may be negative, the total dipolar and quadrupolar cross-sections must be positive putting constraints on the values of  $\sigma^D(l, m)$  and  $\sigma^Q(l, m)$ . The electric field  $\hat{\epsilon}$  and wavevector  $\hat{k}$  coordinates in the  $(\hat{x}, \hat{y}, \hat{z})$  basis of Figure 1 are given by:

$$\hat{\epsilon} = \begin{pmatrix} \sin \theta \cos \phi \\ \sin \theta \sin \phi \\ \cos \theta \end{pmatrix}, \quad \hat{k} = \begin{pmatrix} \cos \theta \cos \phi \\ \cos \theta \sin \phi \\ -\sin \theta \end{pmatrix}. \quad (4)$$

Hence the detail of the cross-section angular dependence in equations 1 and 2 requires the estimate of the spherical tensors  $\sigma^D(l, m)$  and  $\sigma^Q(l, m)$  as performed elsewhere [44]. The XAS cross-section measured experimentally is an average over equivalent Ti atoms under the symmetry operations of the crystal space group. The analytical formula representing this averaged cross-section requires the site symmetrization and crystal symmetrization of the spherical tensors, which is provided in SI § and §. From this analysis, we obtain nearly equal (up to a sign difference) crystal-symmetrized ( $\langle\langle\sigma(l, m)\rangle\rangle_X$ ), site-symmetrized ( $\langle\langle\sigma(l, m)\rangle\rangle$ ) and standard ( $\sigma(l, m)$ ) spherical tensors. Assuming pure 3d and 4p final states in the one-electron approximation, analytical expressions are provided for  $\sigma^D(\hat{\epsilon})$  and  $\sigma^Q(\hat{\epsilon}, \hat{k})$  whose angular dependence with  $\theta$  and  $\phi$  are given in Table II. The full expressions of the cross-sections are provided in SI §. In this paper, we analyze the angular dependence of the pre-edge peak intensities with  $\theta$  and  $\phi$  and assign them to specific final states corresponding to Ti-3d and/or 4p orbitals with the support of both FDM and spherical tensor analysis.

## RESULTS

The experimental evolution of the Ti K-edge spectra with  $\theta$  is depicted in Figure 2a. The spectra are normalized at 4988.5 eV where the cross-section is expected to be  $\theta$ -independent

TABLE II. Angular dependence along  $\theta$  and  $\phi$  of the dipole and quadrupolar XAS cross-section dominant terms in the expansions (1) and (2) at the Ti K-edge of a-TiO<sub>2</sub> according to the final state of the transition. Transitions to  $p$  final states are dipole allowed ( $\sigma^D(\hat{\epsilon})$ ) while transitions to  $d$  final states are quadrupole allowed ( $\sigma^Q(\hat{\epsilon}, \hat{k})$ ).

<b>final state</b>	$\sigma^D(\hat{\epsilon})$ or $\sigma^Q(\hat{\epsilon}, \hat{k})$ $\theta$ - <b>dependence</b>	$\sigma^D(\hat{\epsilon})$ or $\sigma^Q(\hat{\epsilon}, \hat{k})$ $\phi$ - <b>dependence</b>
$p_x, p_y$	$-\cos^2 \theta$	no dependence
$p_z$	$\cos^2 \theta$	no dependence
$d_{z^2}$	$\sin^2 \theta \cdot \cos^2 \theta$	no dependence
$d_{xy}$	$\sin^2 \theta \cdot \cos^2 \theta$	$\cos(4\phi)$
$d_{x^2-y^2}$	$\sin^2 \theta \cdot \cos^2 \theta$	$-\cos(4\phi)$
$d_{xz}, d_{yz}$	$-\sin^2 \theta \cdot \cos^2 \theta$	no dependence

according to FDMNES calculations (shown by the leftmost black arrow in Figure 2b). From this normalization procedure, a series of energy points with cross-section independent of the  $\theta$  angle appear in the experimental dataset, as predicted by the theory (black arrows in Figure 2a and 2b) showing the reliability of the normalization procedure. In the pre-edge, the amplitude of peak A1 is dramatically affected by the sample orientation. In the post-edge regions, significant changes are observed as well.

*Ab-initio* FDM calculations of the total XAS cross-section (including dipolar and quadrupolar terms) are presented in Figure 2b for the same angles of incidence  $\theta$  as in the experiment. In the pre-edge region, the trends for peak A1 and A3 are nicely reproduced. The absence of peak A2, originating from defects [7, 18–20], is due to our perfect crystal modelling in the FDM calculations. In the post-edge region, a good agreement is found especially for the isosbestic points. This shows that a strong LD remains well above the edge in this material.

The evolution of the spectra is also shown for a fixed incidence angle  $\theta = 45^\circ$  while the sample is rotated around  $\phi$  (Figure 3a)[45]. We observe a minimal evolution for the amplitudes of the peak B and at the rising edge from 4971 eV while a larger effect is distinguished in the spectral region of peaks A1, A2 and A3. *Ab-initio* calculations with the same  $\hat{\epsilon}$  and  $\hat{k}$  orientations as in the experiment are depicted in Figure 3b. Only a weak evolution of the amplitude of the pre-edge features is expected and is essentially located in the region of

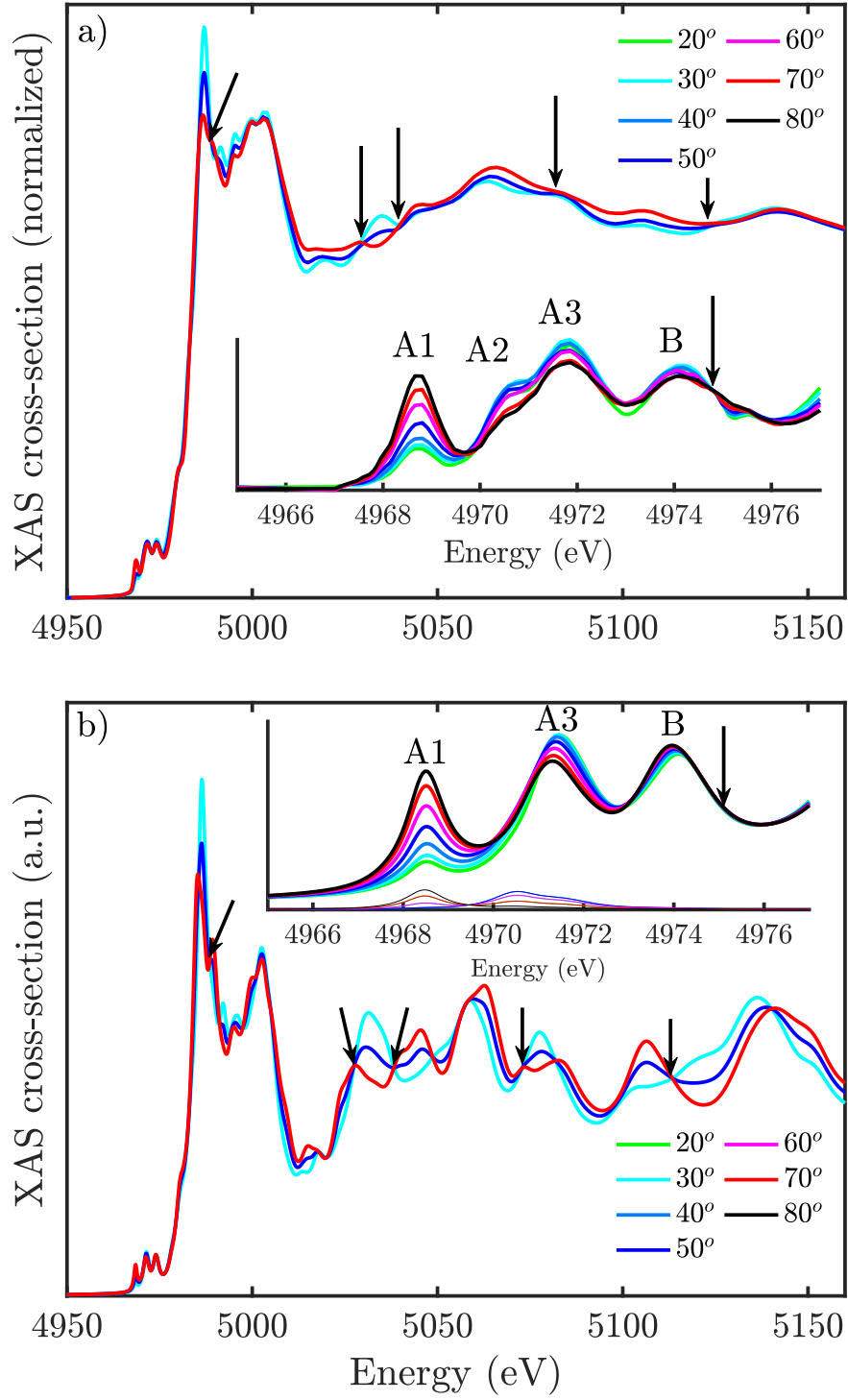


FIG. 2. a) Experimental and b) calculated XAS spectra for different incidence  $\theta$  angles with the sum of dipolar and quadrupolar components (thick lines) and with quadrupolar components only (thin lines in the inset of b)). A few points with  $\theta$ -independent cross-sections are marked with black arrows.

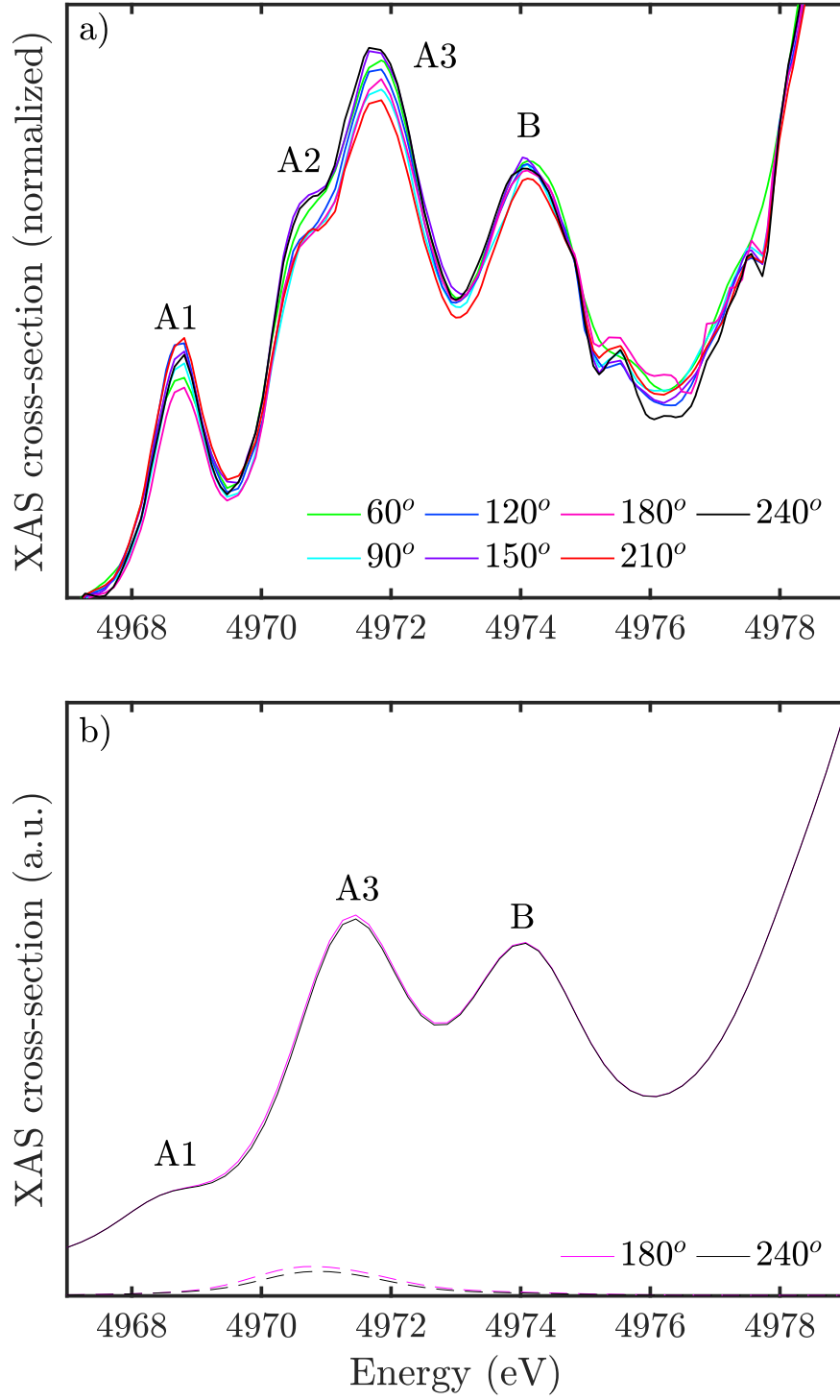


FIG. 3. a) Experimental and b) calculated XAS spectra for different sample orientations along  $\phi$  ( $\theta = 45^\circ$ ) with the sum of dipolar and quadrupolar components (thin lines) and with quadrupolar components only (thin dashed lines in b)). Only two spectra are shown in b) with steps of  $30^\circ$  because the spectra are the same with a periodicity of  $90^\circ$ .

peaks A2 and A3. The amplitude should reach its maximum for  $\phi = 180^\circ [90^\circ]$  which is inconsistent with the experiment. Instead the fitted evolution of the pre-edge peak amplitudes shows that A2 undergoes a 30% peak amplitude change whose angular variation is compatible with a quadrupolar transition (SI Figure 11a) while A1, A3 and B have a maximum amplitude evolution of 10% (within the fitting confidence interval) with no specific periodicity (SI Figure 12). The strong variation in A2 peak amplitude can be observed by the appearance of a pronounced shoulder for  $\phi = 150^\circ$  which becomes smoother for  $\phi = 180^\circ$ . Consequently, the main evolution is due to peak A2 which explains the disagreement with the perfect crystal FDM calculations. It also shows the essentially dipolar content of peaks A1, A3 and B which provide circles in polar plots along  $\phi$  (SI Figure 12) which we show is in agreement with the results obtained from  $\theta$ -scans. A fit of the A2 peak with a  $90^\circ$ -periodic function shows that it may be assigned to the contribution of  $d_{x^2-y^2}$  orbitals from the expected angular evolution by spherical harmonic analysis (SI Figure 11a,b). However, the  $d_{x^2-y^2}$  density of states (DOS) in the region of peak A2 is negligible with respect to  $d_{xy}$  and  $d_{z^2}$  (*vide supra*) hence we rely on the more pronounced angular evolution with  $\theta$  in the following to show the involvement of  $d_{xy}$  orbitals in the formation of peak A2.

In order to describe the origin of the LD with  $\theta$  and assign the pre-edge resonances, the projected DOS of the final states for the pre-edge and post-edge region is depicted in Figure 4 (we drop the term "projected" in the following for simplicity). Due to the large differences between the DOS of  $s$ ,  $p$  and  $d$  states, a logarithmic scale is used vertically and normalized to the orbital having the largest DOS contributing to the final state among  $s$ ,  $p$  and  $d$  orbitals. For peaks A1, A3 and B, most of the DOS comes from  $d$ -orbitals while  $s$ - and  $p$ -DOS are comparable. However, due to the angular momentum selection rule, the spectrum resembles the  $p$ -DOS as witnessed by the similarity between the integrated  $p$ -DOS and the calculated spectrum (black line in Figure 4e). Importantly, peak A1 has only  $(p_x, p_y)$  contributions meaning that this transition is expected to have a much weaker intensity when the electric field gets parallel to the  $\hat{z}$  axis, in agreement with the  $\theta$ -dependence of its amplitude (Figure 2). The  $d$ -DOS at peak A1 involves  $d_{xz}$ ,  $d_{yz}$  and  $d_{x^2-y^2}$  orbitals, among which the first two can hybridize with the  $(p_x, p_y)$  orbitals and relax the dipole selection rules. The dipolar nature of A1 is also seen from the monotonic increase of its amplitude from  $\theta = 0^\circ$  to  $\theta = 90^\circ$ , inconsistent with a quadrupolar allowed transition with  $90^\circ$  periodicity. Following the same analysis, peaks A3 and B do not undergo a strong change in amplitude under  $\theta$ -rotation

because  $(p_x, p_y)$  and  $p_z$  contribute similarly to the DOS for these transitions although FDM calculations show that A3 should evolve in intensity with  $\theta$  due to a  $\sim 20\%$  larger DOS for  $p_z$  than for  $p_x, p_y$  as experimentally observed. From the integrated  $d$ -DOS along  $(x, y)$  and  $z$  (SI Figure 14a), we notice the inconsistency between the peak amplitudes in the theory and the experiment, which shows that they are essentially determined by the  $p$ -DOS (SI Figure 14b).

For a more quantitative description of the dipolar and quadrupolar components in the pre-edge, we extracted the quadrupolar cross-section from FDM calculations. It is depicted as thin lines in the inset of Figure 2b. The quadrupolar contributions are limited to peaks A1 and A3 with a small contribution in the spectral region of peak A2. At peak A1, the quadrupolar amplitude is maximum for  $\theta = 0^\circ$  and  $\theta = 90^\circ$  and the total cross-section becomes mainly quadrupolar for  $\theta = 0^\circ$  while the quadrupolar component contributes  $\sim 15\%$  of the peak amplitude for  $\theta = 90^\circ$ . From the development of the cross-section into spherical harmonics (Table II), the dipolar transitions to  $p_{x,y}$  final states are expected to vary as  $\cos^2 \theta$  while transitions to  $p_z$  vary as  $-\cos^2 \theta$  plus a constant (see SI Figure 17a). The fitted evolution of the dipolar cross-section of peak A1 in the experiment and in the FDM calculations is compatible with a transition to  $p_{x,y}$  (green line in Figure 5a, fitting details in SI §). The quadrupolar component (red line in Figure 5a) is compatible with a transition to  $d_{xz}, d_{yz}$  due to its  $-\sin^2 \theta \cos^2 \theta$  predicted evolution in agreement with the  $d$ -DOS at peak A1 (Table II and Figure 17b). The comparison between the experimental and theoretical amplitudes of peak A1 (Figure 5a) gives an excellent agreement further confirming that the A1 transition is mostly dipolar to  $p_{x,y}$  final states. Following the same analysis, we find that the evolution of A3 and B amplitudes are expected to have a dominant  $p_z$ -DOS character for the former and  $p_{x,y}$ -DOS for the latter. Since the experimental evolution of their amplitudes is rather weak, it is not possible to retrieve the expected angular behavior experimentally (SI Figure 10).

As pointed out earlier, the quadrupolar cross-section has a doublet structure in the region of peaks A1, A2 and A3 (inset of Figure 2b). The most intense of the two peaks at  $\theta = 45^\circ$  is in the spectral region of peak A2 where the transition involving defects is expected in a-TiO<sub>2</sub> real crystals. A closer look at the fitted evolution of the A2 amplitude with  $\theta$  shows a quadrupolar evolution with maximum value at  $\theta = 45^\circ$  (Figure 5b). This is in agreement with the expected angular evolution of  $d_{z^2}$  and  $d_{xy}$  final states from spherical tensor analysis

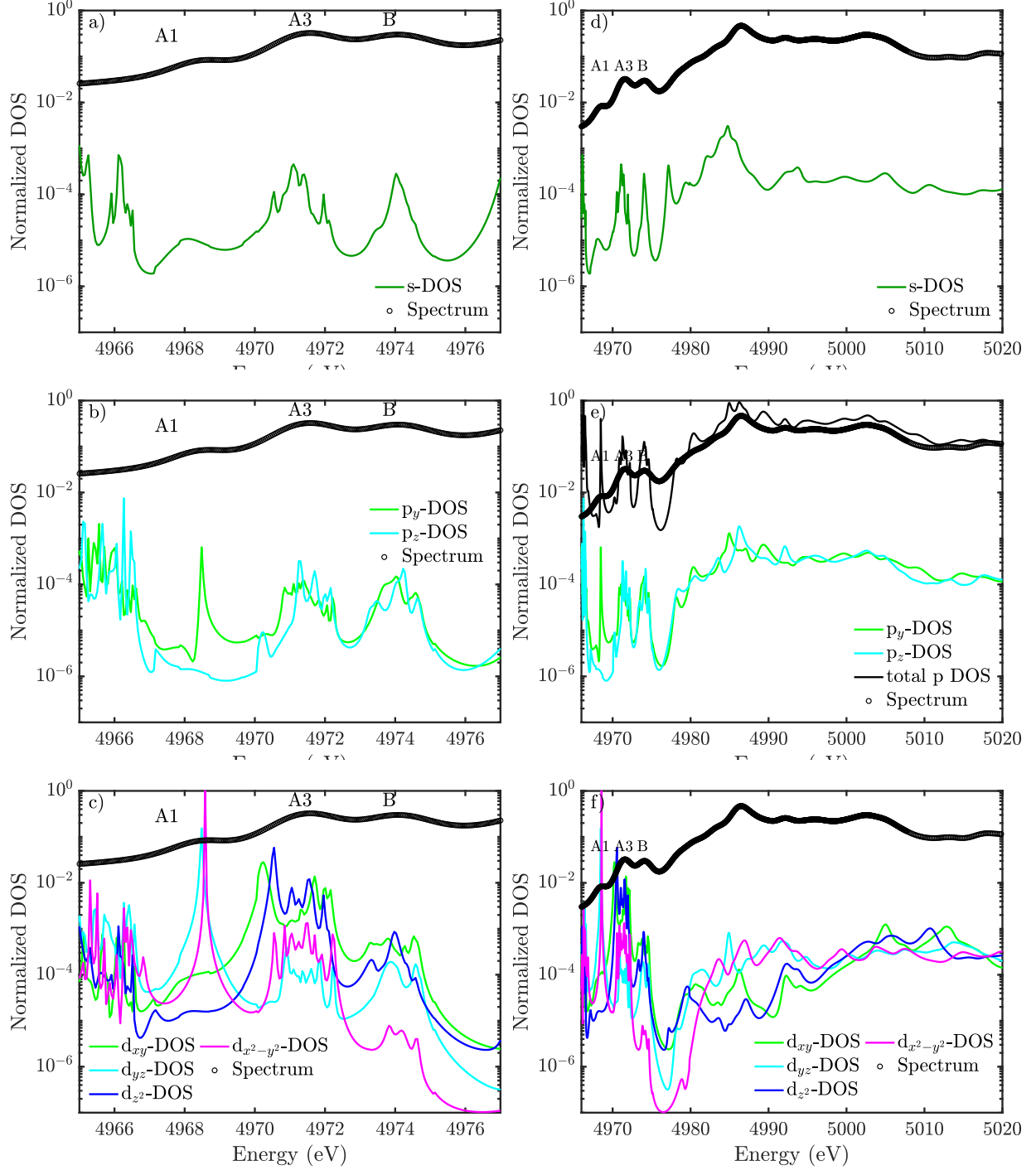


FIG. 4. Calculated projected final state DOS for each type of (a,d)  $s$ -, (b,e)  $p$ - and (c,f)  $d$ -final state orbitals in the pre-edge (left) and post-edge regions (right). Reported spectra (black circles) are calculated for  $\theta = 90^\circ$ . The total  $p$ -DOS ( $p_x, p_y, p_z$ ) is given in e) (black line).

(Figure 17b) which contribute to the DOS in the spectral region of peak A2 (Figure 4c). It

indicates that although the amplitude of A2 is underestimated in the FDM calculation, the consensus that A2 originates from undercoordinated and disordered samples may be more subtle and is discussed in the next section.

From this combined experimental and theoretical analysis, we emphasize that consecutive peaks in the pre-edge of a-TiO<sub>2</sub> are not simply due to the energy splitting between  $t_{2g}$  and  $e_g$  as previously invoked [17]. This splitting is more complicated than the usual octahedral crystal field splitting because of the strong hybridization between  $p$  and  $d$  orbitals in a lowered symmetry environment which affects the relative ordering of the transitions. The consistent results between experiment, FDM calculations and spherical tensor analysis show the reliability of the assignment provided in this work. Table I compares our results with previous assignments of peaks A1 to B.

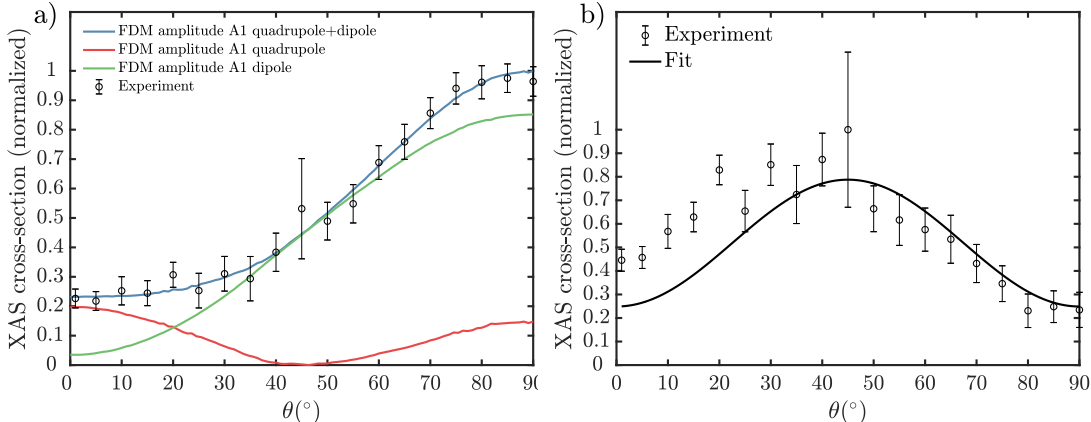


FIG. 5. Overlap between the angular evolution of the amplitudes for peaks a) A1, b) A2 in the theory (lines) and the experiment (circles with error bars). The error bars represent 95% of confidence interval for the fitting of the amplitude.

## DISCUSSION

### Local versus non-local character of the pre-edge transitions

Pre-edge transitions can originate either from on-site (localized) or off-site transitions involving neighbour Ti atoms of the absorber. Off-site transitions are dipole allowed due to the strong  $p - d$  orbital hybridization [16]. This effect has been shown on NiO, an

antiferromagnetic (AF) charge-transfer insulator, for which the Ni K-edge transition to  $3d$  orbitals of the majority spin of the absorber is only possible between Ni sites due to the AF ordering [27]. Hence, to disentangle between the local or non-local character of the pre-edge transitions in a-TiO<sub>2</sub>, we performed FDM calculations on clusters with increasing number of neighbour shells starting from an octahedral TiO<sub>6</sub> cluster with the same geometry and bond distances as in the bulk. The results are shown in SI Figure 13 with two orthogonal electric field orientations along [001] ( $\theta = 0^\circ$ ) and [010] ( $\theta = 90^\circ$ ).

The calculation for TiO<sub>6</sub> (green curve) shows only A1 meaning that it is mostly an on-site transition. The absence of peaks A3 and B suggests that they are mostly non-local transitions in agreement with Ref. [17]. Increasing the cluster size to 4 Å includes the second shell of Ti ions, which generates most of the A3 amplitude. This shows that, similarly to NiO, an energy gap opens between the on-site and off-site transitions to  $3d$  orbitals of Ti and that A3 is mostly dipolar and strongly influenced by the intersite  $3d - 4p$  hybridization. Peak B is missing for this cluster size which shows that it is due to a longer range interaction and can be reconstructed with a 5 Å cluster including the next shell of neighbor Ti atoms.

### Origin of peak A2

The experimental  $\phi$  and  $\theta$  angular evolution of the A2 amplitude (Figure 5b and 11a in the SI) matches a quadrupolar transition, qualitatively consistent with the cross-section obtained from FDMNES calculations (Figure 2b, inset and Figure 3b). Since it has been concluded that A2 is related to lattice defects [7, 18–20, 22, 23, 26], the question arises as to the physical details of this origin. Because of its essentially quadrupolar character, a likely reason for the underestimated A2 amplitude in the theory is due to the fact that a perfect lattice has been considered. The occurrence of an oxygen vacancy in the vicinity of a Ti atom will further lower the  $D_{2d}$  symmetry and introduce  $p - d$  orbital mixing in the pentacoordinated Ti atom increasing the transition amplitude while the angular dependence of the A2 peak remains mainly quadrupolar. The dipolar component introduced by this process may explain the deviation of the experimental points in Figure 5b from the "perfect" quadrupolar dependence between the points at  $\theta = 0^\circ$  to  $\theta = 90^\circ$ . This interpretation does not take into account the possible spectral distribution changes occurring in the pre-edge for the pentacoordinated Ti atoms. In order to check the effect of an O<sub>vac</sub> on the XAS spectrum

of a Ti atom in the vicinity, *ab-initio* FDM calculations are performed at the Ti K-edge of Ti atoms with an  $O_{\text{vac}}$  at the apical or equatorial position in a supercell of 51 atoms [46]. The results, depicted in Figure 6, show a chemical shift of A1 peak in the region between peaks A1 and A3 of the perfect lattice where peak A2 is expected, while peaks A3 and B remain essentially unaffected by the  $O_{\text{vac}}$ . The shift of peak A1 is explained from the essentially local character of its final state involving  $3d$  orbitals in the final state of the quadrupolar transition sensitive to the core-hole. The  $O_{\text{vac}}$  generates a redistribution of the electrons among the three coordinated Ti atoms which better screen the core-hole charge and lead to a blue shift of the transition. Since peaks A3 and B involve the first and second coordination shell of Ti atoms, the effect of the  $O_{\text{vac}}$  on the final state is likely negligible on the corresponding final states. Further energy shift is expected from polaronic effects upon formation of  $Ti^{3+}$  centres and associated lattice relaxation similar to other systems [47, 48]. In this interpretation, the experimental spectrum of a-TiO<sub>2</sub> would be a linear combination of the  $O_{\text{vac}}$  spectra (red and blue curves in Figure 6) and the spectrum of hexacoordinated Ti atoms in the bulk (black curve in Figure 6) which depends on the amount of vacancy in the system. Peak A2 can be viewed as a peak A1 replica undergoing a blue shift under the influence of an  $O_{\text{vac}}$ . For pentacoordinated Ti atoms, the calculations show a reduction of the XAS cross-section in the region of peak A1 and a strong enhancement in the region of peak A2 which is fully compatible with our recent studies on photoexcited a-TiO<sub>2</sub> nanoparticles [22, 23, 26]. The transient spectrum shows a transfer of spectral weight from a bulk a-TiO<sub>2</sub> to amorphous TiO<sub>2</sub> structure which increases significantly the A2 peak amplitude. We therefore conclude that the intensity enhancement at the peak A2 originates from the combination of a relaxed quadrupolar in the regular lattice and from the spectral shift of peak A1 in the region of peak A2 for pentacoordinated Ti atoms with an  $O_{\text{vac}}$ .

## CONCLUSION

In summary, a complementary approach using experimental LD measurements at the Ti K-edge of a-TiO<sub>2</sub>, *ab-initio* FDM calculations and spherical tensor analysis provides an unambiguous assignment of the pre-edge features. The distinction between on-site and off-site transitions is possible using different cluster sizes in the FDM calculations. The LD is visible well above the absorption edge due to the strong  $p$ -orbital polarization in a-TiO<sub>2</sub> which

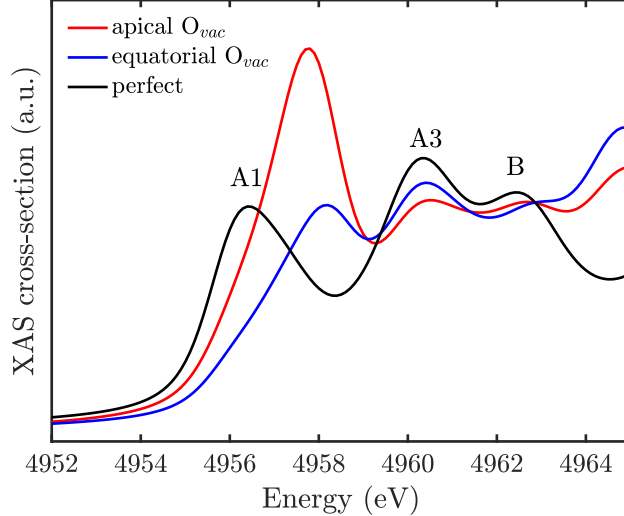


FIG. 6. Effect of an oxygen vacancy introduced at the equatorial (blue) or apical position (red) of a  $\text{TiO}_6$  octahedron on the XAS spectrum of a  $\text{TiO}_2$  supercell. The spectrum at the Ti K-edge for the perfect supercell is shown in black. The calculation is angle averaged (no specific orientation taken for the crystal and the incident X-ray beam).

affects the amplitude of the EXAFS through an anisotropy of the single scattering terms. Surprisingly, a quadrupolar angular evolution is observed for peak A2. A connection between the unexpectedly large experimental amplitude of this peak is made with oxygen vacancies forming pentacoordinated Ti atoms, which adds a small amount of dipolar components via  $p-d$  orbital mixing. In addition, crude FDMNES calculations show that A2 may be viewed as a A1 peak undergoing a blue shift because of the change in the core hole screening due to  $\text{O}_{\text{vac}}$ 's. Experiments are on-going to extend this work to rutile  $\text{TiO}_2$ .

The present results and analysis should be cast in the context of ongoing ultrafast X-ray spectroscopy studies at Free Electron Lasers [49, 50]. For materials such as a- $\text{TiO}_2$ , the increased degree of detail that can be gathered from such sources was nicely illustrated in a recent paper by Obara et al. [24] on a- $\text{TiO}_2$ , showing that the temporal response of the pure electronic feature (at the Ti K-edge) was much faster ( $\sim 100$  fs) than the response of structural features ( $\sim 330$  fs) such as the pre-edge and the above-edge XANES. The present work shows that by exploiting the angular dependence of some of the features, even up to the EXAFS region, one could get finer details about the structural dynamics, in particular, of non equivalent displacements of nearest neighbours.

T.C.R would like to thank Yves Joly and Christian Brouder for fruitful discussions and

Hengzhong Zhang for providing the FDMNES input files. We thank the NCCR: MUST of the Swiss NST and the ERC Grant DYNAMOX for support. We thank Beat Meyer and Mario Birri from the microXAS beamline for their technical support as well as the Bernina staff at the SwissFEL for providing the goniometer stage.

---

- [1] M. Freitag, J. Teuscher, Y. Saygili, X. Zhang, F. Giordano, P. Liska, J. Hua, S. M. Zakeeruddin, J.-E. Moser, M. Grätzel, and A. Hagfeldt, *Nature Photonics* **11**, 372 (2017).
- [2] K. Nakata and A. Fujishima, *Journal of Photochemistry & Photobiology, C: Photochemistry Reviews* **13**, 169 (2012).
- [3] K. Suenaga, M. Tencé, C. Mory, C. Colliex, H. Kato, T. Okazaki, H. Shinohara, K. Hirahara, S. Bandow, and S. Iijima, *Science* **290**, 2280 (2000).
- [4] J. F. Sherson, C. Weitenberg, M. Endres, M. Cheneau, I. Bloch, and S. Kuhr, *Nature* **467**, 68 (2010).
- [5] C. J. Milne, T. J. Penfold, and M. Chergui, *Coordination Chemistry Reviews* **277-278**, 44 (2014).
- [6] C. Brouder, D. Cabaret, A. Juhin, and P. Sainctavit, *Physical Review B* **81**, 432 (2010).
- [7] V. Luca, *The Journal of Physical Chemistry C* **113**, 6367 (2009).
- [8] R. Brydson, H. Sauer, W. Engel, J. M. Thomass, E. Zeitler, N. Kosugi, and H. Kuroda, *Journal of Physics: Condensed Matter* **1**, 797 (1999).
- [9] T. Uozumi, K. Okada, A. Kotani, O. Durmeyer, J. P. Kappler, E. Beaurepaire, and J. C. Parlebas, *EPL (Europhysics Letters)* **18**, 85 (1992).
- [10] Z. Y. Wu, G. Ouvrard, P. Gressier, and C. R. Natoli, *Physical Review B* **55**, 10382 (1997).
- [11] D. W. Fischer, *Physical Review B* **5**, 4219 (1972).
- [12] M. F. Ruiz-Lopez and A. Munoz-Paez, *Journal of Physics: Condensed Matter* **3**, 8981 (1991).
- [13] L. A. Grunes, *Physical Review B* **27**, 2111 (1983).
- [14] F. Farges, G. E. Brown, and J. J. Rehr, *Physical Review B* **56**, 1809 (1997).
- [15] C. A. Triana, C. M. Araujo, R. Ahuja, G. A. Niklasson, and T. Edvinsson, *Physical Review B* **94**, 165129 (2016).
- [16] T. Yamamoto, *X-Ray Spectrometry* **37**, 572 (2008).
- [17] D. Cabaret, A. Bordage, A. Juhin, M. Arfaoui, and E. Gaudry, *Physical Chemistry Chemical*

- Physics **12**, 5619 (2010).
- [18] L. X. Chen, T. Rajh, Z. Wang, and M. C. Thurnauer, *The Journal of Physical Chemistry B* **101**, 10688 (1997).
- [19] V. Luca, S. Djajanti, and R. F. Howe, *The Journal of Physical Chemistry B* **102**, 10650 (1998).
- [20] T. L. Hanley, V. Luca, I. Pickering, and R. F. Howe, *The Journal of Physical Chemistry B* **106**, 1153 (2002).
- [21] H. Zhang, B. Chen, J. F. Banfield, and G. A. Waychunas, *Physical Review B* **78**, 528 (2008).
- [22] M. H. Rittmann-Frank, C. J. Milne, J. Rittmann, M. Reinhard, T. J. Penfold, and M. Chergui, *Angewandte Chemie International Edition* **53**, 5858 (2014).
- [23] F. G. Santomauro, A. Lübcke, J. Rittmann, E. Baldini, A. Ferrer, M. Silatani, P. Zimmermann, S. Grübel, J. A. Johnson, S. O. Mariager, P. Beaud, D. Grolimund, C. Borca, G. Ingold, S. L. Johnson, and M. Chergui, *Scientific Reports* **5**, 1 (2015).
- [24] Y. Obara, H. Ito, T. Ito, N. Kurahashi, S. Thürmer, H. Tanaka, T. Katayama, T. Togashi, S. Owada, Y.-i. Yamamoto, S. Karashima, J. Nishitani, M. Yabashi, T. Suzuki, and K. Misawa, *Structural Dynamics* **4**, 044033 (2017).
- [25] E. Baldini, L. Chiodo, A. Dominguez, M. Palummo, S. Moser, M. Yazdi-Rizi, G. Auböck, B. P. P. Mallett, H. Berger, A. Magrez, C. Bernhard, M. Grioni, A. Rubio, and M. Chergui, *Nature Communications* **8**, 37 (2017).
- [26] J. Budarz, F. G. Santomauro, M. H. Rittmann-Frank, C. J. Milne, T. Huthwelker, D. Grolimund, J. Rittmann, D. Kinschel, T. Rossi, and M. Chergui, *CHIMIA International Journal for Chemistry* **71**, 768 (2017).
- [27] C. Gougoussis, M. Calandra, A. Seitsonen, C. Brouder, A. Shukla, and F. Mauri, *Physical Review B* **79**, 045118 (2009).
- [28] Y. Joly, O. Bunău, J. E. Lorenzo, R. M. Galéra, S. Grenier, and B. Thompson, *Journal of Physics: Conference Series* **190**, 012007 (2009).
- [29] Y. Joly, *Physical Review B* **63**, 125120 (2001).
- [30] C. Brouder, J. P. Kappler, and E. Beaurepaire, *Conference Proceedings - 2nd European Conference on Progress in X-ray Synchrotron Radiation Research* **25**, 19 (1990).
- [31] B. Henke, E. Gullikson, and J. Davis, *Atomic Data and Nuclear Data Tables* **54**, 181 (1993).
- [32] G. N. George, R. C. Prince, T. G. Frey, and S. P. Cramer,

- Physica B-Condensed Matter **158**, 81 (1989).
- [33] G. Louprias, S. Rabii, J. Tarbès, S. Nozières, and R. C. Tatar, Physical Review B **41**, 5519 (1990).
- [34] H. Oyanagi, M. Tokumoto, T. Ishiguro, H. Shirakawa, H. Nemoto, T. Matsushita, and H. Kuroda, Synthetic Metals **17**, 491 (1987).
- [35] H. Oyanagi, K. Oka, H. Unoki, Y. Nishihara, K. Murata, T. Matsushita, M. Tokumoto, and Y. Kimura, Physica B-Condensed Matter **158**, 436 (1989).
- [36] R. F. Pettifer, C. Brouder, M. Benfatto, C. R. Natoli, C. Hermes, and M. Lopez, Physical Review B **42**, 37 (1990).
- [37] S. Stizza, M. Benfatto, A. Bianconi, J. García, G. Mancini, and C. R. Natoli, Le Journal de Physique Colloques **47**, C8 (1986).
- [38] C. Frétnigny, D. Bonnin, and R. Cortes, Le Journal de Physique Colloques **47**, C8 (1986).
- [39] For a spectrum measured well above the absorption edge, the atomic background absorption converges for any incident polarization and can also be used in principle to renormalize the spectra.
- [40] R. Carboni, S. Giovannini, G. Antonioli, and F. Boscherini, Physica Scripta **2005**, 986 (2005).
- [41] Y. Joly, D. Cabaret, H. Renevier, and C. R. Natoli, Physical Review Letters **82**, 2398 (1999).
- [42] L. Hedin and B. I. Lundqvist, Journal of Physics C: Solid State Physics **4**, 2064 (2001).
- [43] C. Brouder, Journal of Physics: Condensed Matter **2**, 701 (1990).
- [44] C. Brouder, A. Juhin, A. Bordage, and M.-A. Arrio, Journal of Physics: Condensed Matter **20**, 455205 (2008).
- [45] The normalization energy is at 4988.5 eV.
- [46] The calculations are performed with a bulk  $\alpha$ -TiO<sub>2</sub> 3x3x2 lattice structure and no lattice relaxation is included under the formation of a neutral O<sub>vac</sub>.
- [47] A. Janotti and C. G. Van de Walle, Applied Physics Letters **87**, 122102 (2005).
- [48] T. J. Penfold, J. Szlachetko, F. G. Santomauro, A. Britz, W. Gawelda, G. Doumy, A. M. March, S. H. Southworth, J. Rittmann, R. Abela, M. Chergui, and C. J. Milne, Nature Communications **9**, 1 (2018).
- [49] R. Abela, P. Beaud, J. A. van Bokhoven, M. Chergui, T. Feurer, J. Haase, G. Ingold, S. L. Johnson, G. Knopp, H. Lemke, C. J. Milne, B. Pedrini, P. Radi, G. Schertler, J. Standfuss, U. Staub, and L. Patthey, Structural Dynamics **4**, 061602 (2017).

[50] M. Chergui, *Structural Dynamics* **3**, 031001 (2016).

X-ray Absorption Linear Dichroism at the Ti K-edge of TiO<sub>2</sub>

anatase single crystal  
Supplementary Information

## SAMPLE GROWTH AND CHARACTERIZATIONS

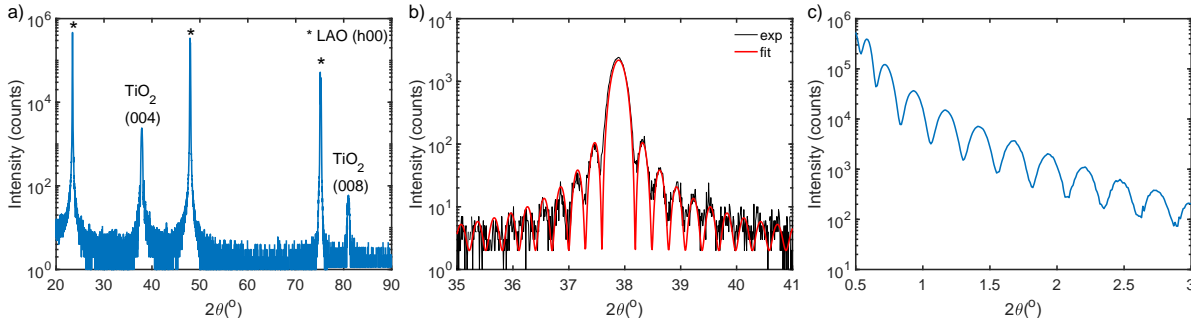


FIG. 7. a) X-ray diffraction pattern from the (001)-anatase  $\text{TiO}_2$  thin film, b) X-ray interferences in the region of diffraction peak (004) (black) and fitting to the interference fringes (red) showing a sample thickness of  $31 \pm 1$  nm, c) X-ray reflectometry showing a sample thickness of  $32.8 \pm 0.1$  nm.

(001)-oriented epitaxial thin films of anatase  $\text{TiO}_2$  are fabricated by pulse laser deposition (PLD). The vacuum chamber has a base pressure of about  $10^{-5}$  Pa. A KrF excimer laser (Lambda Physik LPX 300, 25 ns pulses,  $\lambda = 248$  nm) was used to ablate a target material of  $\text{TiO}_2$  fabricated in our laboratory. Commercially available (100)-oriented  $\text{LaAlO}_3$  (LAO) single crystal ( $10 \times 10 \times 0.5$  mm) were used as substrates. The target to substrate distance was set at 40 mm and the laser energy at the target was about 32 mJ on a spot area of about  $1.6 \text{ mm}^2$  which gives an energy density of about  $2.0 \text{ J/cm}^2$ . The films were grown under oxygen partial pressure of 5 Pa. Platinum paste was used to provide the thermal contact between the substrate and the heating stage. The substrate temperature was about  $610(\pm 10)^\circ\text{C}$ , as measured with a pyrometer pointing at a Pt black spot near the substrate. X-ray diffraction (XRD) and X-ray reflectometry (XRR) (PANalytical X’pert Pro MPD with  $\text{Cu K}\alpha_1$  radiation at  $1.540 \text{ \AA}$ ) analyses were used to investigate the crystalline structure of the films and for the calibration of the deposition rate, respectively. XRD shows the (001)-orientation of the deposited anatase  $\text{TiO}_2$  thin film (Figure 7a). Besides the (h00) reflexes of the substrate, only two diffraction peaks are visible identified to the (004) and (008) reflexes of anatase  $\text{TiO}_2$  (001)-oriented epitaxially on (100)-LAO. Interference fringes near the (004) diffraction peak are fitted to provide a film thickness of  $31 \pm 1$  nm (Figure 7b). The Kiessig fringes observed in XRR provide a sample thickness of  $32.8 \pm 0.1$  nm (Figure 7c) in agreement with XRD.

## FITTING OF THE PRE-EDGE PEAK AMPLITUDES

The pre-edge peak amplitudes were fitted in `Matlab` with a set of five gaussians for the experimental data and a set of four pseudo-Voight lineshapes for the calculated spectra. Overlap between the spectra and the fits are shown in Figure 8 for  $\theta$ -scans and Figure 9 for  $\phi$ -scans. Fittings of individual spectra (at a given angle) are shown in Figure ?? for  $\theta$ -scans and Figure ?? for  $\phi$ -scans. The spectra amplitudes do not match between the experiment and the theory because the experiment deals with a number of photons detected by an APD in a given emission cone while the calculations provide transition amplitudes so that a normalization procedure was performed based on the isosbestic points with  $\theta$  (at  $E = 4988.5$  eV).

Since the absolute amplitudes of the XAS in the theory and the experiment are not comparable, the experimental fitted amplitudes are rescaled in amplitude and offset to find the best agreement with the theory in Figure 5a in the main text and in Figure 10 of the SI.

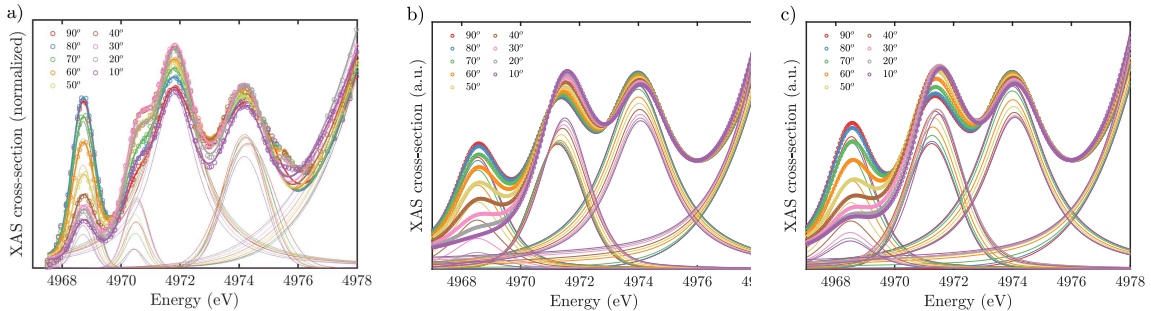


FIG. 8. Fitting of a) experimental, b) theoretical dipole and c) theoretical dipole+quadrupole pre-edge features of  $\alpha$ - $\text{TiO}_2$  with a) five gaussians, b) and c) four pseudo-Voight functions for different angles of incidence  $\theta$ .

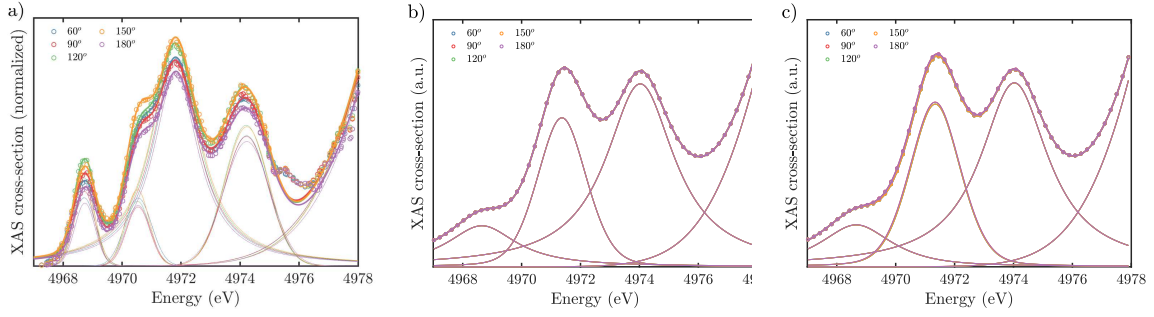


FIG. 9. Fitting of a) experimental, b) theoretical dipole and c) theoretical dipole+quadrupole pre-edge features of a-TiO<sub>2</sub> with a) five gaussians, b) and c) four pseudo-Voigt functions for different rotation angles  $\phi$  and with an angle of incidence  $\theta = 45^\circ$ .

## EVOLUTION OF THE A2, A3 AND B PEAK AMPLITUDES WITH $\theta$ AND $\phi$

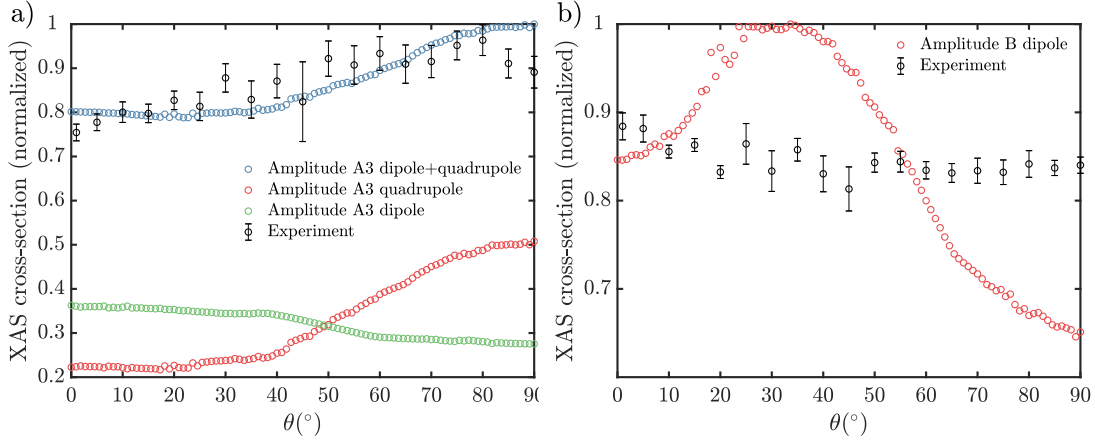


FIG. 10. Evolution of a) A3 and b) B peak amplitudes when going from  $\theta = 0^\circ$  ( $\hat{\epsilon} \parallel [001], \hat{k} \parallel [100]$ ) to  $\theta = 90^\circ$  ( $\hat{\epsilon} \parallel [100], \hat{k} \parallel [00 - 1]$ ). Error bars provide 95% confidence interval for the fitting.

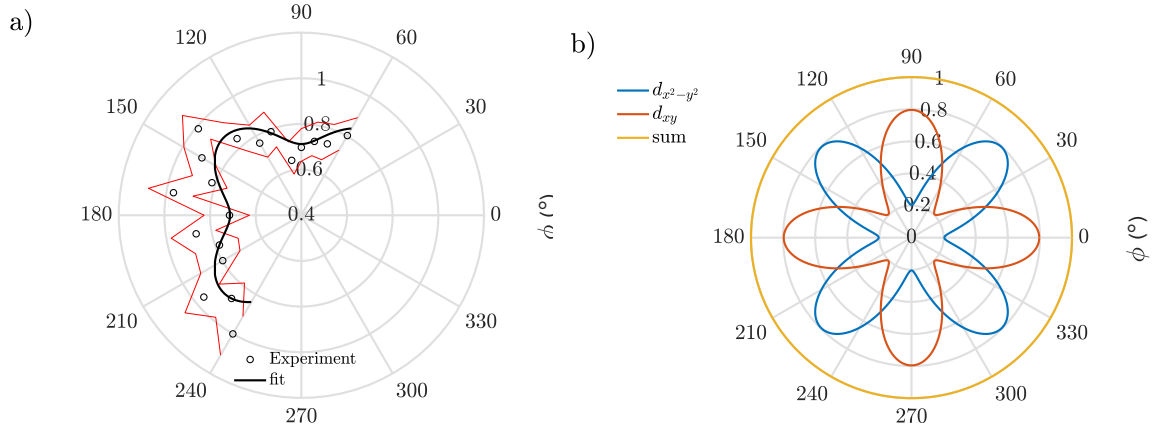


FIG. 11. a) Normalized evolution of the peak A2 amplitude when rotating the crystal with  $\phi$  in the  $([100], [010])$  plane with an incidence angle  $\theta = 45^\circ$ . The red lines represent the boundaries of 95% confidence interval of the experimental fittings to the A2 peak amplitude. The black line is a fitting to the experimental data with a periodic function of  $\cos 4\phi$  corresponding to a quadrupolar evolution. b) Theoretical evolution of the XAS quadrupolar cross-section with angle  $\phi$  assuming a given final state.

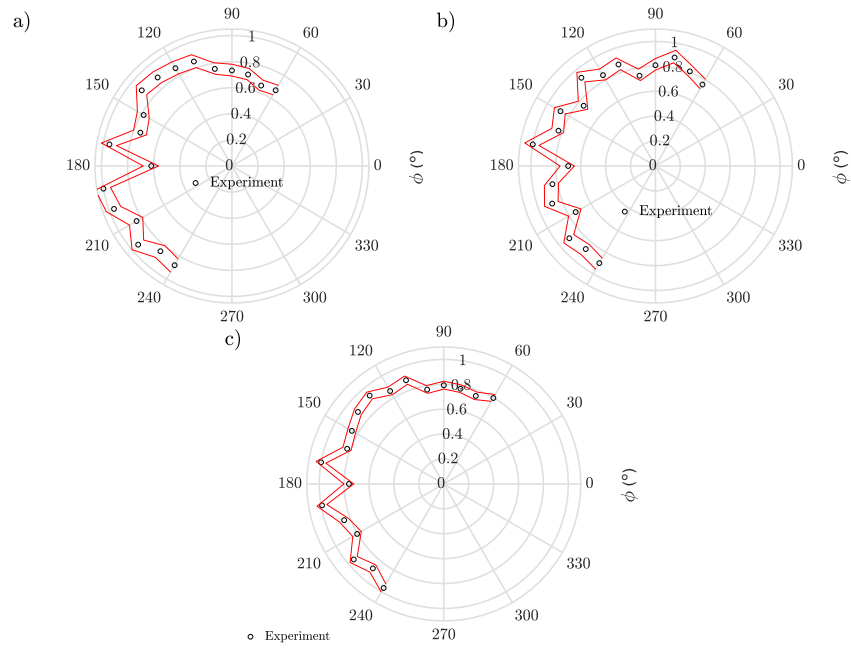


FIG. 12. Normalized evolution of peak a) A1, b) A3 and c) B amplitudes when rotating the crystal with  $\phi$  in the  $([100], [010])$  crystal plane. The red lines represent the boundaries of 95% confidence interval of the experimental fittings to the peak amplitudes.

## FDMNES CALCULATIONS FOR DIFFERENT CLUSTER SIZES

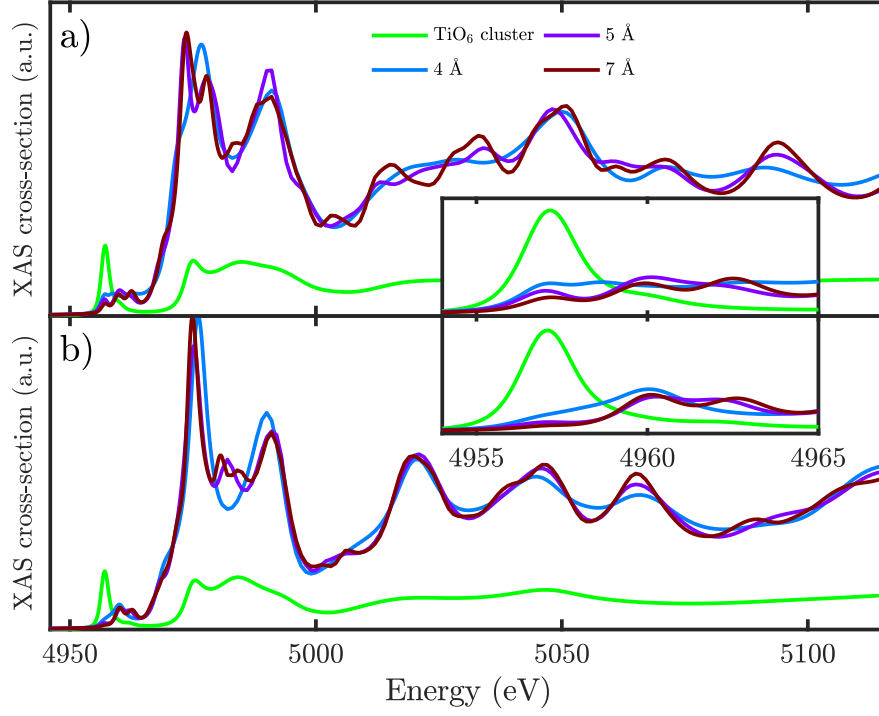


FIG. 13. Evolution of the calculated a-TiO<sub>2</sub> XAS spectrum with cluster size in the FDM calculation for a)  $\theta = 90^\circ$  ( $\hat{\epsilon} \parallel [010], \hat{k} \parallel [00 - 1]$ ), b)  $\theta = 0^\circ$  ( $\hat{\epsilon} \parallel [001], \hat{k} \parallel [100]$ ).

# INTEGRATED DOS ALONG $x$ AND $y$ AXES

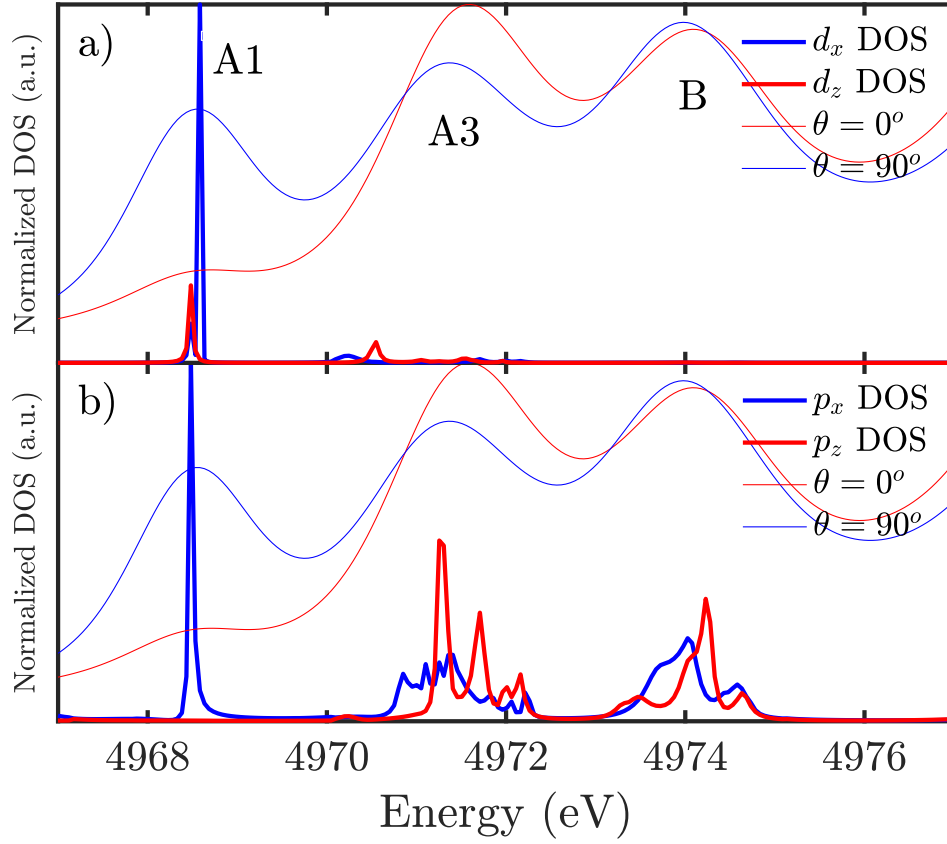


FIG. 14. Projected DOS along  $x$  and  $z$  in the pre-edge for a)  $d$ -orbitals and b)  $p$ -orbitals (thick lines) and calculated spectra for incidence angles  $\theta = 0^\circ$  (red thin line) and  $\theta = 90^\circ$  (blue thin line).

## XAS SPECTRUM OF A GIVEN SITE

The unit cell of  $\alpha$ -TiO<sub>2</sub> has two equivalent Ti sites (actually four equivalent sites but connected with the  $(1/2, 1/2, 1/2)$  translation). The calculation of the XAS spectrum with FDMNES at each site is shown in Figure 15 for  $\theta = 45^\circ$  and Figure 16 for  $\phi = 0^\circ$  and  $90^\circ$  which show that both sites provide the same spectra.

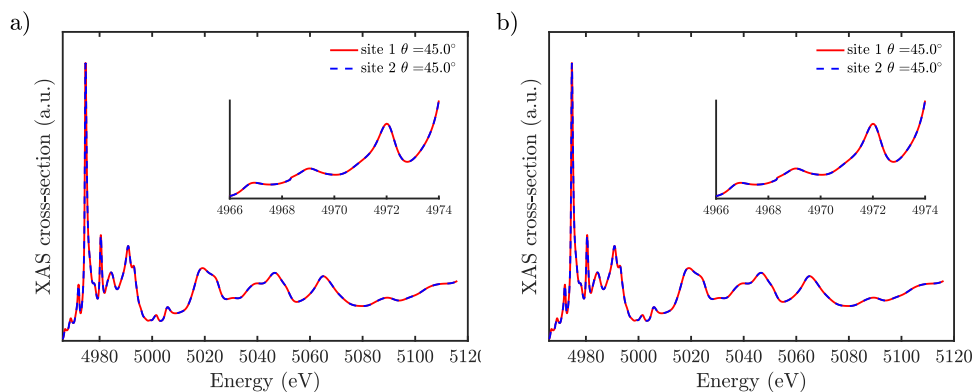


FIG. 15. Difference between the spectra calculated at the different Ti sites for an incidence angle  $\theta = 0^\circ$  showing no difference between the sites. a) Dipole component, b) Dipole and quadrupole components. The spectra are not convoluted to the experimental resolution.

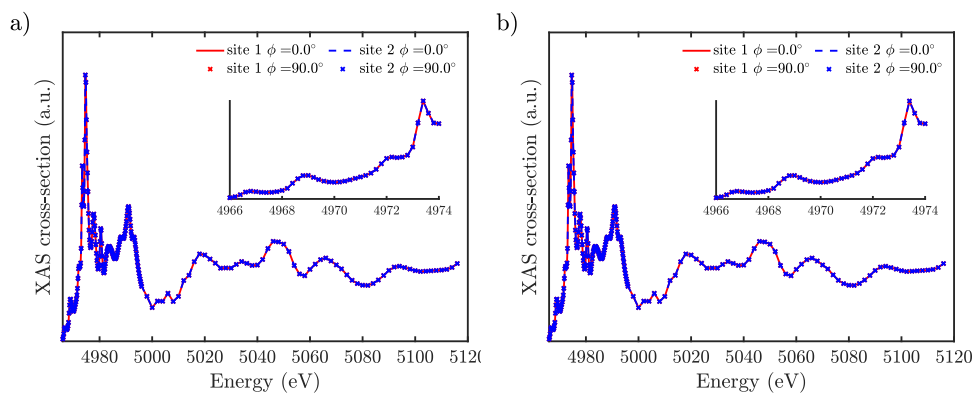


FIG. 16. Difference between the spectra calculated at the different Ti sites for different rotation angles  $\phi$  showing no difference between the sites. a) Dipole component only, b) Sum of dipole and quadrupole components. The spectra are not convoluted to the experimental resolution.

## CRYSTAL-SYMMETRIZATION OF THE SPHERICAL TENSORS

First, the spherical tensors are symmetrized in the Ti site frame and then in the crystal frame taking into account the possible equivalent sites in the unit cell. The experimentally measured XAS spectrum is the average over the equivalent Ti sites.

### Derivation of the site-symmetrized spherical tensors of anatase in the site frame

The local point group of anatase is  $D_{2d}$  (subgroup of the crystal point group  $D_{4h}$ ) which contains 4 pure rotations ( $E, C_2(z), C'_2(x), C'_2(y)$ ) and 4 rotoinversions (the same as the pure rotations combined with the inversion). The angular evolution of the dipole and quadrupole cross-sections in this point group are the same as in the crystal point group  $D_{4h}$  following for the dipole cross-section

$$\sigma^D(\hat{\epsilon}) = \sigma^D(0, 0) - \frac{1}{\sqrt{2}}(3 \cos^2 \theta - 1)\sigma^D(2, 0) \quad (5)$$

and for the quadrupole cross-section,

$$\begin{aligned} \sigma^Q(\hat{\epsilon}, \hat{k}) &= \sigma^Q(0, 0) + \sqrt{\frac{5}{14}}(3 \sin^2 \theta \sin^2 \psi - 1)\sigma^Q(2, 0) \\ &+ \frac{1}{\sqrt{14}}[35 \sin^2 \theta \cos^2 \theta \cos^2 \psi + 5 \sin^2 \theta \sin^2 \psi - 4]\sigma^Q(4, 0) \\ &+ \sqrt{5} \sin^2 \theta [(\cos^2 \theta \cos^2 \psi - \sin^2 \psi) \cos 4\phi - 2 \cos \theta \sin \psi \cos \psi \sin 4\phi] \sigma^{Qr}(4, 4) \end{aligned} \quad (6)$$

The site frame has the  $\hat{z}$  axis chosen along the elongated axis of the  $\text{TiO}_6$  octahedron and the  $\hat{x}$  and  $\hat{y}$  axes bisectors of the equatorial Ti–O bonds to form a direct frame. The site-symmetrized spherical tensor  $\langle \sigma(l, m) \rangle$  in the site frame is given by:

$$\langle \sigma(l, m) \rangle = \frac{1}{|G'|} \sum_g \epsilon(g) \sum_{m'=-l}^{m'=l} \sigma(l, m') D_{m'm}^l(g) \quad (7)$$

with  $|G'| = 8$  the number of rotoinversions and pure rotations in the site point group,  $g$  a rotoinversion in the site point group, and  $D_{m'm}^l$  a Wigner-D matrix element. The parity factor is  $\epsilon(g) = -1$  when the spherical tensor is odd and the symmetry operation  $g$  contains the inversion or  $\epsilon(g) = 1$  otherwise. The Euler angles of the pure rotations are  $E : (0, 0, 0)$ ,  $C_2(z) : (0, 0, \pi)$ ,  $C'_2(x) : (0, -\pi, \pi)$  and  $C'_2(y) : (0, -\pi, 0)$  while for the corresponding rotations combined with the inversion we get  $(0, -\pi, \pi)$ ,  $(0, -\pi, 0)$ ,  $(0, 0, 0)$

and  $(0, 0, \pi)$  which represent two times a set of four Euler angles. This provides the following symmetrized dipolar spherical tensors in the site frame:

$$\begin{aligned}\langle \sigma^D(0, 0) \rangle &= \frac{1}{8} \sum_g \epsilon(g) \sigma^D(0, 0) D_{00}^0(g) = \sigma^D(0, 0) \\ \langle \sigma^D(2, 0) \rangle &= \frac{1}{8} \sum_g \sum_{m'=-2}^{m'=2} \epsilon(g) \sigma^D(2, m') D_{m'0}^2(g) = \sigma^D(2, 0)\end{aligned}\tag{8}$$

and the following quadrupolar spherical tensors,

$$\begin{aligned}\langle \sigma^Q(0, 0) \rangle &= \frac{1}{8} \sum_g \sigma^Q(0, 0) D_{00}^0(g) = \sigma^Q(0, 0) \\ \langle \sigma^Q(2, 0) \rangle &= \frac{1}{8} \sum_g \sum_{m'=-2}^{m'=2} \sigma^Q(2, m') D_{m'0}^2(g) = \sigma^Q(2, 0) \\ \langle \sigma^Q(4, 0) \rangle &= \frac{1}{8} \sum_g \sum_{m'=-4}^{m'=4} \sigma^Q(4, m') D_{m'0}^4(g) = \sigma^Q(4, 0) \\ \langle \sigma^Q(4, 4) \rangle &= \frac{1}{8} \sum_g \sum_{m'=-4}^{m'=4} \sigma^Q(4, m') D_{m'4}^4(g) = \frac{1}{2} (\sigma^Q(4, 4) + \sigma^Q(4, -4)) = \Re \sigma^Q(4, 4)\end{aligned}\tag{9}$$

where we have used time reversal symmetry for  $\langle \sigma^Q(4, 4) \rangle$ .

### From site-symmetrized spherical tensors to crystal-symmetrized spherical tensors

The coset method is a powerful way to calculate the spherical tensors averaged over the crystal from the spherical tensor symmetrized over a single site which has been developed by Brouder and coworkers [44]. The crystal-symmetrized tensor  $\langle \sigma(l, m) \rangle_X$  of a given site is obtained from the *site-symmetrized tensor*  $\langle \sigma(l, m) \rangle$  by the operation

$$\langle \sigma(l, m) \rangle_X = \frac{1}{n} \sum_{i=1}^n \sum_{m'=-l}^{m'=l} \epsilon(g_i) \langle \sigma(l, m) \rangle D_{m'm}^l(g_i^{-1})\tag{10}$$

with  $n$  the number of cosets and  $g_i$  a symmetry operation between the equivalent Ti sites. Briefly, the subgroup of  $I4_1/amd$  (group 141 with choice of origin number 1) with periodic translations has 8 symmetry operations which leave the Ti site at  $(0, 0, 0)$  invariant:  $(x, y, z)$ ,  $(-x, -y, -z)$ ,  $(-x, y, z)$ ,  $(x, -y, z)$ ,  $(y, -x, z)$ ,  $(-y, x, z)$ ,  $(-y, -x, -z)$  and  $(y, x, -z)$  which gives  $n = |I4_1/amd|/|D_{2d}| = 32/8 = 4$  equivalent sites. However, the translation  $(1/2, 1/2, 1/2)$  gives the same orientation for the Ti site at the center of the unit

cell that at the corner and as they will give the same XAS spectra, we only need to consider 2 equivalent sites. The sites at  $(0, 0, 0)$  and  $(0, 1/2, 1/4)$  are considered which are connected to each other with the representative of the cosets  $(x, y, z)$  and  $(-y, x + \frac{1}{2}, z + \frac{1}{4})$ . The symmetry operation which allows going from one site to the other is defined by the matrix  $R_{eq}$ ,

$$R_{eq} = \begin{pmatrix} 0 & -1 & 0 \\ 1 & 0 & 0 \\ 0 & 0 & 1 \end{pmatrix} \quad (11)$$

with inverse rotation which needs to be considered in equation 10,

$$R_{eq}^{-1} = \begin{pmatrix} 0 & 1 & 0 \\ -1 & 0 & 0 \\ 0 & 0 & 1 \end{pmatrix} \quad (12)$$

which corresponds to the Euler angles  $(0, 0, -\pi/2)$  in ZYZ convention. The relation to go from the sWe can now calculate the crystal symmetrized spherical tensors:

$$\begin{aligned} \langle \sigma(0, 0) \rangle_X &= \frac{1}{2} \sum_{i=1}^2 \langle \sigma(l, m) \rangle D_{m'm}^l(g_i^{-1}) = \langle \sigma(0, 0) \rangle \\ \langle \sigma(2, 0) \rangle_X &= \langle \sigma(2, 0) \rangle \\ \langle \sigma(4, 0) \rangle_X &= \langle \sigma(4, 0) \rangle \\ \langle \sigma(4, 4) \rangle_X &= \langle \sigma(4, 4) \rangle \end{aligned} \quad (13)$$

which are very simple relations. However, be careful at this point since the site-symmetrized tensors appearing of the righthand side of the equations are in the crystal frame. We can convert them into the site frame using the equation:

$$\langle \sigma(l, m) \rangle_2 = \sum_{m'=-l}^l \langle \sigma(l, m') \rangle_1 D_{m'm}^l(g) \quad (14)$$

where  $g$  is the symmetry operation to go from frame 1 to frame 2. The transformation to go from the crystal frame to the site frame is represented by the matrix,

$$\begin{pmatrix} \frac{\sqrt{2}}{2} & -\frac{\sqrt{2}}{2} & 0 \\ \frac{\sqrt{2}}{2} & \frac{\sqrt{2}}{2} & 0 \\ 0 & 0 & 1 \end{pmatrix} \quad (15)$$

with the corresponding Euler angles  $(0, 0, \pi/4)$  in ZYZ convention. Hence we get,

$$\begin{aligned}
\langle \sigma(0, 0) \rangle_X &= \langle \sigma(0, 0) \rangle \\
\langle \sigma(2, 0) \rangle_X &= \langle \sigma(2, 0) \rangle \\
\langle \sigma(4, 0) \rangle_X &= \langle \sigma(4, 0) \rangle \\
\langle \sigma(4, 4) \rangle_X &= -\langle \sigma(4, 4) \rangle
\end{aligned} \tag{16}$$

We notice only a sign change for the  $\langle \sigma(4, 4) \rangle_X$  matrix element. The relations of the spherical tensors in anatase remain simple. From these calculations, we also conclude that the two equivalent sites of Ti considered in the crystal-symmetrization have actually the same spectrum since they are rotated by  $\pi$  around the  $\hat{x}$  or  $\hat{y}$  axis of the crystal which does not change the relative orientation of the  $p$  or  $d$  orbitals involved in the transitions. Consequently, crystal-symmetrized, site-symmetrized and standard spherical tensors can be used interchangeably (except  $\sigma(4, 4)$ ). We checked the equivalence between the sites with FDMNES calculations and both dipole and quadrupole components measured under any  $\theta$  or  $\phi$  angle have the same cross-sections for both sites. The symmetrized spherical tensors have to be used in equations 5 and 6 to obtain the angular evolution of the dipole and quadrupole cross-section remembering that the angles present in these equations are referenced in the site frame. This leaves the angle  $\theta$  unchanged because the  $\hat{z}$  axis is the same in the site frame or in the crystal frame but the  $\phi$  angle in the crystal frame is  $\phi + \frac{\pi}{4}$  in the site frame. Consequently, the expression of the dipole cross-section is unchanged while the expression of the quadrupole cross-section is given by,

$$\cos(\phi + \frac{\pi}{4}) = \frac{\sqrt{2}}{2}(\cos \phi - \sin \phi), \quad \sin(\phi + \frac{\pi}{4}) = \frac{\sqrt{2}}{2}(\cos \phi + \sin \phi) \tag{17}$$

and provide the expression for the quadrupole cross-section (only the last term undergoes a sign change),

$$\begin{aligned}
\sigma^Q(\hat{\epsilon}, \hat{k}) &= \sigma^Q(0, 0) + \sqrt{\frac{5}{14}}(3 \sin^2 \theta \sin^2 \psi - 1)\sigma^Q(2, 0) \\
&+ \frac{1}{\sqrt{14}}[35 \sin^2 \theta \cos^2 \theta \cos^2 \psi + 5 \sin^2 \theta \sin^2 \psi - 4]\sigma^Q(4, 0) \\
&- \sqrt{5} \sin^2 \theta[(\cos^2 \theta \cos^2 \psi - \sin^2 \psi) \cos 4\phi - 2 \cos \theta \sin \psi \cos \psi \sin 4\phi]\sigma^{Qr}(4, 4)
\end{aligned} \tag{18}$$

The expression of the spherical tensor elements is given in Table IV assuming a given final state  $3d$  orbital and provide the relative amplitude between the terms of  $\sigma^Q(\hat{\epsilon}, \hat{k})$ .

## SPHERICAL TENSORS OF ANATASE

final state	$\sigma^D(0, 0)$	$\sigma^D(2, 0)$
$p_x$	$2/\sqrt{5}$	$2/\sqrt{14}$
$p_y$	$2/\sqrt{5}$	$2/\sqrt{14}$
$p_z$	$2/\sqrt{5}$	$-2/\sqrt{14}$

TABLE III. Table of dipolar spherical tensors based on the reached final state. Each element of the table must be multiplied by  $\alpha\hbar\omega\delta(E_f - E_i - \hbar\omega)\xi_f^2$  where  $f$  is the final state reached by the transition which represents the integration of the radial parts of the wavefunctions.

final state	$\sigma^Q(0, 0)$	$\sigma^Q(2, 0)$	$\sigma^Q(2, 2)$	$\sigma^Q(4, 0)$	$\sigma^Q(4, 2)$	$\sigma^{Qr}(4, 4)$	$\sigma^{Qr}(4, -4)$
$d_{z^2}$	$2/\sqrt{5}$	$-4/\sqrt{14}$	0	$12/\sqrt{70}$	0	0	0
$d_{x^2-y^2}$	$2/\sqrt{5}$	$4/\sqrt{14}$	0	$2/\sqrt{70}$	0	1	1
$d_{xy}$	$2/\sqrt{5}$	$4/\sqrt{14}$	0	$2/\sqrt{70}$	0	-1	-1
$d_{xz}$	$2/\sqrt{5}$	$-2/\sqrt{14}$	$-\sqrt{3/7}$	$-8/\sqrt{70}$	$2/\sqrt{7}$	0	0
$d_{yz}$	$2/\sqrt{5}$	$-2/\sqrt{14}$	$\sqrt{3/7}$	$-8/\sqrt{70}$	$-2\sqrt{7}$	0	0

TABLE IV. Table of quadrupolar spherical tensors based on the reached final state. Each element of the table must be multiplied by  $\alpha\hbar\omega k^2\delta(E_f - E_i - \hbar\omega)\xi_f^2$  where  $f$  is the final state reached by the transition which represents the integration of the radial parts of the wavefunctions.

### Final expression of the dipole cross-section

$$\sigma^D(\hat{\epsilon}) = \sigma^D(0, 0) - \frac{1}{\sqrt{2}}(3 \cos^2 \theta - 1)\sigma^D(2, 0) \quad (19)$$

*Final state is  $p_z$*

$$\sigma^D(\hat{\epsilon}) \propto \alpha\hbar\omega \left( \frac{2}{\sqrt{5}} - \frac{1}{\sqrt{7}}(3 \cos^2 \theta - 1) \right) \xi_{z^2}^2 \delta(E_f - E_i - \hbar\omega) \quad (20)$$

*Final state is  $p_x$  or  $p_y$*

$$\sigma^D(\hat{\epsilon}) \propto \alpha \hbar \omega \left( \frac{2}{\sqrt{5}} + \frac{1}{\sqrt{7}} (3 \cos^2 \theta - 1) \right) \xi_{x,y}^2 \delta(E_f - E_i - \hbar \omega) \quad (21)$$

**Final expression of the quadrupole cross-section as a function of  $\theta$**

$$\begin{aligned} \sigma^Q(\hat{\epsilon}, \hat{k}) &= \sigma^Q(0, 0) + \sqrt{\frac{5}{14}} (3 \sin^2 \theta \sin^2 \psi - 1) \sigma^Q(2, 0) \\ &+ \frac{1}{\sqrt{14}} [35 \sin^2 \theta \cos^2 \theta \cos^2 \psi + 5 \sin^2 \theta \sin^2 \psi - 4] \sigma^Q(4, 0) \\ &- \sqrt{5} \sin^2 \theta [(\cos^2 \theta \cos^2 \psi - \sin^2 \psi) \cos 4\phi - 2 \cos \theta \sin \psi \cos \psi \sin 4\phi] \sigma^{Qr}(4, 4) \end{aligned} \quad (22)$$

In the configuration of the experiment,  $\psi = 0$  and  $\phi = \pi/2$ . Hence the dominant term in the expansion is the third term proportional to  $\sigma^Q(4, 0)$  or  $\sigma^{Qr}(4, 4)$  depending on the final state orbital.

*Final state is  $d_{z^2}$*

$$\sigma^Q(\hat{\epsilon}, \hat{k}) \propto \alpha \hbar \omega k^2 \left( \frac{2}{\sqrt{5}} + \frac{1}{7\sqrt{5}} (35 \sin^2 \theta \cos^2 \theta - 4) \right) \xi_{z^2}^2 \delta(E_f - E_i - \hbar \omega) \quad (23)$$

*Final state is  $d_{xy}$*

$$\sigma^Q(\hat{\epsilon}, \hat{k}) \propto \alpha \hbar \omega k^2 \left( \frac{2}{\sqrt{5}} + \frac{1}{42\sqrt{5}} (35 \sin^2 \theta \cos^2 \theta - 4) + \sqrt{5} \sin^2 \theta \cos^2 \theta \right) \xi_{xy}^2 \delta(E_f - E_i - \hbar \omega) \quad (24)$$

*Final state is  $d_{x^2-y^2}$*

$$\sigma^Q(\hat{\epsilon}, \hat{k}) \propto \alpha \hbar \omega k^2 \left( \frac{2}{\sqrt{5}} + \frac{1}{42\sqrt{5}} (35 \sin^2 \theta \cos^2 \theta - 4) - \sqrt{5} \sin^2 \theta \cos^2 \theta \right) \xi_{x^2-y^2}^2 \delta(E_f - E_i - \hbar \omega) \quad (25)$$

*Final state is  $d_{xz}$  or  $d_{yz}$*

$$\sigma^Q(\hat{\epsilon}, \hat{k}) \propto \alpha \hbar \omega k^2 \left( \frac{2}{\sqrt{5}} - \frac{2}{21\sqrt{5}} (35 \sin^2 \theta \cos^2 \theta - 4) \right) \xi_{yz}^2 \delta(E_f - E_i - \hbar \omega) \quad (26)$$

**Final expression of the quadrupole cross-section as a function of  $\phi$**

In the configuration of this experiment,  $\theta = \frac{\pi}{4}$ .

*Final state is  $d_{z^2}$ ,  $d_{xz}$ ,  $d_{yz}$*

Since these final states have  $\sigma^{Qr}(4, 4) = 0$ , they do not depend on  $\phi$  according to equation 22.

*Final state is  $d_{x^2-y^2}$*

$$\sigma^Q(\hat{\epsilon}, \hat{k}) \propto \alpha \hbar \omega k^2 \left( \frac{71\sqrt{5}}{168} - \frac{\sqrt{5}}{4} \cos 4\phi \right) \xi_{x^2-y^2}^2 \delta(E_f - E_i - \hbar \omega) \quad (27)$$

*Final state is  $d_{xy}$*

$$\sigma^Q(\hat{\epsilon}, \hat{k}) \propto \alpha \hbar \omega k^2 \left( \frac{71\sqrt{5}}{168} + \frac{\sqrt{5}}{4} \cos 4\phi \right) \xi_{xy}^2 \delta(E_f - E_i - \hbar \omega) \quad (28)$$

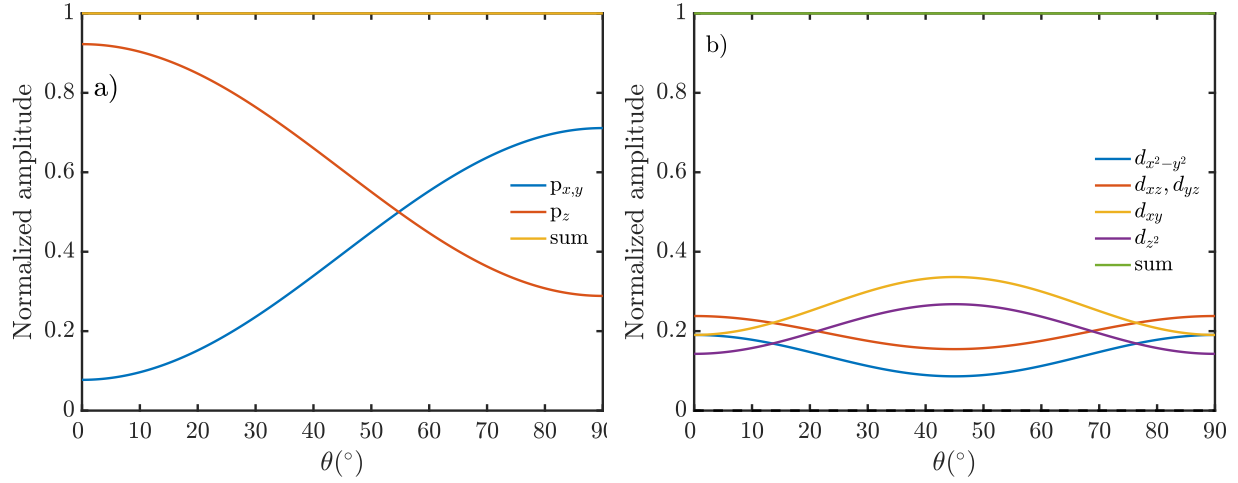


FIG. 17. Normalized evolution of the a) dipolar and b) quadrupolar cross-section with the angle of incidence  $\theta$  in the configuration of the experiment for different final states.